Oil & Natural Gas Technology

Detection and Production of Methane Hydrate

Semi-annual Progress Report

Reporting Period: November, 2008-April, 2009

Submitted by:
Rice University and University of Houston

George J. Hirasaki and Walter Chapman, Chemical and Biomolecular Engineering
Gerald R. Dickens, Colin A. Zelt, and Brandon E. Dugan, Earth Science
Kishore K. Mohanty, University of Houston

May, 2009

DOE Award No.: DE-FC26-06NT42960

Rice University – MS 362
6100 Main St.
Houston, TX 77251-1892
Phone: 713-348-5416; FAX: 713-348-5478; Email: gjh@rice.edu

University of Houston
Department of Chemical Engineering
4800 Calhoun Street
Houston, TX 77204-4004

Prepared for:
United States Department of Energy
National Energy Technology Laboratory

Office of Fossil Energy

Table of Contents

Disclaimer

Executive Summary

Task 5: Carbon Inputs and Outputs to Gas Hydrate Systems

The abundance and distribution of gas hydrate in marine sediment sequences depend on inputs and outputs of carbon over time. The primary input is solid organic carbon, which is converted to methane. The primary outputs for many systems are anaerobic oxidation of methane and gas burial. The primary scope of this task is to generate chemical constraints on carbon inputs and outputs, which can be incorporated into numerical models. We have generated almost all data and are beginning to incorporate into models.

Task 6: Numerical Models for Quantification of Hydrate and Free Gas Accumulations

Accumulation of gas hydrate and free gas is modeled in heterogeneous marine sediments over geologic time scales. The two-dimensional numerical model incorporates deposition and compaction of heterogeneous sediments, methane generation, and migration of water with dissolved gas. Fracture network systems and dipping sand layers are common examples of lithologic heterogeneities in natural gas hydrate systems, and are simulated using the current 2-D model. Increased fluid flux within these high permeability conduits results in concentrated hydrate deposits.

The upward flux of methane is an important determinant for the amount of hydrate that may potentially be present in the sediments. One approach to measure methane flux is to relate sulfate methane transition (SMT) depth to the methane flux via anaerobic oxidation of methane (AOM). Dickens suggests that AOM is the most dominant reaction in natural gas hydrate systems. However, numerous prominent authors such as Kastner *et al*. argue that consumption of pore water sulfate in shallow sediments is a result of oxidation of particulate organic carbon (POC) and not methane (Kastner et al., 2008). The articles in *Fire in the Ice* by Kastner *et al*., 2008 and Dickens and Snyder, 2009 focus on these two important arguments in the gas hydrate community and warrant more detailed modeling to help resolve the questions raised by these prominent groups.

We show some evidence from literature about existence of multiple gas components in hydrate samples, and some well logging data which shows the existence of sII hydrate existing below the traditional Base of sI hydrate Stability Zone. And also we show the synthetic seismic response from a CH_4-C_3H_8-H_2O hydrate system, demonstrating the possibility of a weak BSR.

Task 7: Analysis of Production Strategy

Gas production from unconfined dipping class 2 hydrate reservoirs is studied. Depressurization alone is effective in dipping unconfined reservoirs, but gas production rate is much slower than that for warm water injection. As the injection point of the warm water moves down the reservoir, the start of the high gas recovery phase gets delayed, but the time for completion of gas recovery becomes shorter. The cost of wells and warm water must be optimized along with the gas production to determine the optimal strategy for producing hydrate reservoirs. We also presented a paper in the SPE Reservoir Symposium on history matching of core-scale hydrate formation and dissociation experiments.

Task 8: Seafloor and Borehole Stability

We are moving forward on Task 8 as scheduled. Major advancements have been made on two fronts: (1) modeling (in)stability by looking at active fracture genesis in hydrate settings; and (2) modeling (in)stability by including slope stability calculations during hydrate accumulation (Task 6). In addition to this, we have continued to characterize the permeability behavior of fine-grained sediments including anisotropy and assessing the value of NMR-based permeability estimates in hydrate systems. Other hydrate related activities have been participation in DOE-sponsored site survey analysis for JIP drilling, review of hydrate manuscripts, and presentations at international meetings.

Task 9: Geophysical Imaging of Gas Hydrate and Free Gas Accumulations

The traveltime inversion part of the project is complete. The final results were shown at the US-Korea Methane Hydrate Workshop at Lawrence-Berkeley lab on April 28, 2009. We present the same series of results below. The final traveltime model will be used as a starting model for waveform inversion which is our goal in year 2.

Background

A. Objective

This project seeks to understand regional differences in gas hydrate systems from the perspective of as an energy resource, geohazard, and long-term climate influence. Specifically, the effort will: (1) collect data and conceptual models that targets causes of gas hydrate variance, (2) construct numerical models that explain and predict regional-scale gas hydrate differences in 2- and 3-dimensions with minimal "free parameters", (3) simulate hydrocarbon production from various gas hydrate systems to establish promising resource characteristics, (4) perturb different gas hydrate systems to assess potential impacts of hot fluids on seafloor stability and well stability, and (5) develop geophysical approaches that enable remote quantification of gas hydrate heterogeneities so that they can be characterized with minimal costly drilling. Our integrated program takes advantage of the fact that we have a close working team comprised of experts in distinct disciplines.

The expected outcomes of this project are improved exploration and production technology for production of natural gas from methane hydrates and improved safety through understanding of seafloor and well bore stability in the presence of hydrates.

B. Scope of Work

The scope of this project is to more fully characterize, understand, and appreciate fundamental differences in the amount and distribution of gas hydrate and how this affects the production potential of a hydrate accumulation in the marine environment. The effort will combine existing information from locations in the ocean that are dominated by low permeability sediments with small amounts of high permeability sediments, one permafrost location where extensive hydrates exist in reservoir quality rocks and other locations deemed by mutual agreement of DOE and Rice to be appropriate. The initial ocean locations are Blake Ridge, Hydrate Ridge, Peru Margin and GOM. The permafrost location is Mallik. Although the ultimate goal of the project is to understand processes that control production potential of hydrates in marine settings, Mallik will be included because of the extensive data collected in a producible hydrate accumulation. To date, such a location has not been studied in the oceanic environment. The project will work closely with ongoing projects (e.g. GOM JIP and offshore India) that are actively investigating potentially economic hydrate accumulations in marine settings.

The overall approach is fivefold: (1) collect key data concerning hydrocarbon fluxes which is currently missing at all locations to be included in the study, (2) use this and existing data to build numerical models that can explain gas hydrate variance at all four locations, (3) simulate how natural gas could be produced from each location with different production strategies, (4) collect new sediment property data at these locations that are required for constraining fluxes, production simulations and assessing sediment stability, and (5) develop a method for remotely quantifying heterogeneities in gas hydrate and free gas distributions. While we generally restrict our efforts to the locations where key parameters can be measured or constrained, our ultimate aim is to make our efforts universally applicable to any hydrate accumulation.

Task 5: Carbon Inputs and Outputs to Gas Hydrate Systems

Background

Task 5: Carbon Inputs and Outputs to Gas Hydrate Systems
Responsible Party: *Rice University*

Subtask 5.1. Complete iodine cycling. The recipient shall collect sediment sample cores from Blake Ridge, Peru Margin, Hydrate Ridge and GOM (as well as other promising hydrate accumulation sites deemed appropriate by mutual agreement of the recipient and DOE). The recipient shall wash and freeze-dry sediments to remove pore water, and then measure them for Iodine (I) and Organic Carbon (C_{org}) contents. The recipient shall conduct activities necessary to liberate and analyze the I (liberated by hydropyrolysis, collected in solution, and analyzed by Inductively Coupled Plasma Mass Spectrometry (ICP-MS)). The recipient shall determine the content of C_{org} contents (through use of a CHNO analyzer). The recipient shall quantify how much I is incorporated into C_{org} near the seafloor and returned to pore waters at depth. The recipient shall use this information in conjunction with pore water I^- profiles to constrain the integrated C_{org} flux over time.

Subtask 5.2. Authigenic minerals. The recipient shall collect sediment cores as identified in subtask 5.1, with specific focus on cores across the modern zone of Anaerobic Oxidation of Methane (AOM). After removing pore water, the recipient shall digest sediment aliquots in acetic acid and aqua regia such that the first extraction dissolves carbonate and the second dissolves barite. The recipient shall analyze the solutions for metals (e.g., Ba, Ca, Mg, Sr) using Inductively Coupled Plasma Atomic Emission Spectrometry (ICP-AES). The recipient shall use resulting sedimentary metal profiles to quantify the location and mass of authigenic minerals. The recipient shall use this information in conjunction with pore water chemistry to constrain hydrocarbon outputs through AOM.

Task 5: Carbon Inputs and Outputs to Gas Hydrate Systems

Approach

The amount and distribution of gas hydrate in marine sediment depends on several factors. Our project-related modeling efforts (Bhatnager et al., 2007a, 2008), as well as results from other studies, show that two particularly important factors are: (1) the flux of labile organic carbon over time, and (2) loss of methane via anaerobic oxidation of methane (AOM). We are trying to constrain these factors by generating key chemical data sets using sediment obtained from present-day gas hydrate systems.

Results and Discussion

We have generated a series of iodine profiles for sediment and pore waters through several gas hydrate systems (Blake Ridge, Peru Margin, Gulf of Mexico, Japan Sea). The profiles at Blake Ridge and Peru Margin have a fairly straightforward interpretation. Organic carbon lands on the seafloor with iodine. During burial, iodine is released from the organic carbon, contributing to iodide in pore water. This iodide moves upward toward the seafloor, by diffusion, advection or both. Here, it is converted to iodate and re-scavenged by organic carbon. The consequence is a system where the amount of iodine in pore waters is proportional to carbon input and fluid dynamics over

time. This information can be used in our models. The iodine in the GOM and Japan Sea is not so easy to understand because, so far, it appears that there are external sources of iodine.

We are on the second draft of an iodine paper, which should be submitted in the summer of 2009. We are beginning to incorporate carbon and iodine into our models for gas hydrate formation. The overall idea here is that organic carbon added to the sediment sequence should give a specific gas hydrate profile as well as dissolved inorganic carbon and iodine profiles.

We have generated a series of pore water and sediment data (metals and carbonate) across the sulfate-methane transition at sites with gas hydrate in the Japan Sea and on the Peru Margin. For all sites, there is an obvious sulfate-methane transition (SMT) with high amounts of authigenic carbonate (calcite) and barite. We interpret the SMT at these sites (and at most other gas hydrate locations) as resulting from AOM, and the authigenic mineral fronts as reflecting methane output that has been similar to present-day over a long time (>100,000 years) interval (i.e., steady-state). The results of the Japan Sea have been published (Snyder et al., 2007). The results from the Peru Margin should be published this summer.

Our interpretations contrast with those of some authors. Specifically, we believe that the depth of the SMT is directly related to the loss of methane whereas some authors suggest it results from oxidation of organic carbon. We have written a short article explaining our views and why we think the alternative interpretation is incorrect (Dickens and Snyder, 2009).

We have now calculated sulfate and bicarbonate fluxes at 20 “gas hydrate” sites at 7 locations. These locations span a range of parameters (e.g., water depth, SMT depth, etc.). So far, all data supports our interpretations and assumptions that methane flux can be calculated from sulfate profiles. We are now writing a summary paper on this topic.

We have collected and analyzed samples from a location on the Peru Margin for carbon isotopes. The authigenic carbonates have a d13C of -6 per mil, even though we believe they are the result of AOM. This is because, in our opinion, there is a major upward flux of bicarbonate.

Conclusions

Models concerning the abundance and distribution of gas hydrate in marine sediment require constraints on carbon inputs and outputs, fluid flow and temporal evolution. Our chemical analyses of sediment appear to be providing us interesting constraints that we can use in our models.

Task 6: Numerical Models for Quantification of Hydrate and Free Gas Accumulations

Subtask 6.1: Model development: Sayantan Chatterjee

Accumulation of gas hydrate and free gas is modeled in heterogeneous marine sediments over geologic time scales. The two-dimensional numerical model incorporates deposition and compaction of heterogeneous sediments, methane generation, and migration of water with dissolved gas. Fracture network systems and dipping sand layers are common examples of lithologic heterogeneities in natural gas hydrate systems, and are simulated using the current 2-D model. Increased fluid flux within these high permeability conduits results in concentrated hydrate deposits. Simulations with vertical fracture systems using the two-dimensional model are shown in the following section.

Gas Hydrate Systems with Vertical Fracture Networks

Natural gas hydrate systems have several fracture networks, dominated by focused fluid flow, which act as high permeability conduits and cause localized high concentration of hydrate and free gas within these networks (Weinberger and Brown, 2006). This particular lithologic heterogeneity is usually common in geologic settings such as the Hydrate ridge in the Cascadia Margin varying over different length scales (Trehu et al., 2004; Weinberger and Brown, 2006).

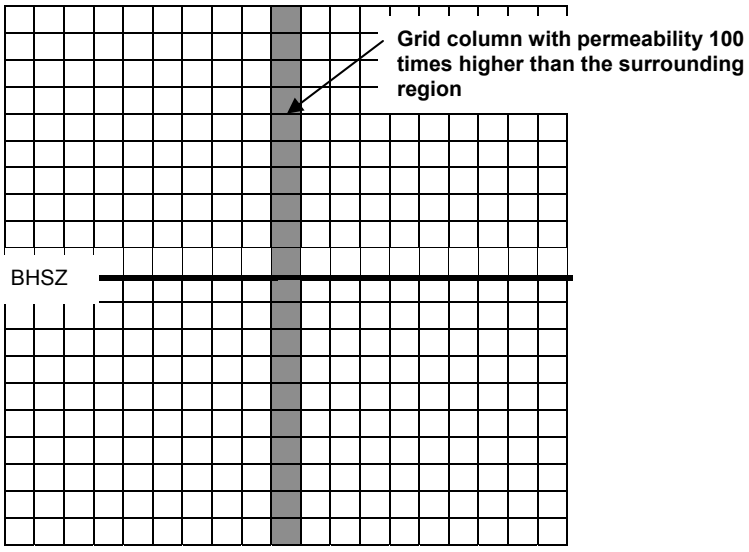

Figure 6.1.1: Permeability map showing initial location of a high permeability vertical fracture network system

As an extension of Bhatnagar's 1-D work, we simulated a vertical fracture system in the 2-D model by assigning higher permeability in different grid blocks along a single column throughout the simulation domain. Vertical fracture networks are modeled from the time they are introduced at $\tilde{t} = 0$ in the system through steady state and follow transient gas hydrate and free gas accumulation with sedimentation and deposition of

the neighboring formation. The initial permeability distribution for the vertical fracture network is shown schematically in figure 6.1.1.

Simulations with a vertical fracture network, 100 times more permeable than the surrounding formation that extends through the gas hydrate stability zone (GHSZ) up to the seafloor are presented using the 2-D model (i.e. $N_{sc} = 20$ for the sediment formation and $N_{sc} = 2000$ for the fracture system). The primary dimensionless transport parameters in our model are assigned as following: $Pe_1 = 0.1$, $Da = 1$, $\beta = 6$, $\gamma = 9$, $\eta = 6/9$, and $N_{t\phi} = 1$. Seafloor parameters, relative permeabilities, capillary pressure and physical properties of water, hydrate and free gas are same as used in the one-dimensional model (Bhatnagar, 2007). The organic content leaving the GHSZ is observed to be dependent on the ratio Pe_1/Da as shown in figure 6.1.2.

$$\frac{Pe_1}{Da} = \frac{U_{f,sed}}{\lambda L_t} = \frac{Sedimentation}{Reaction}$$

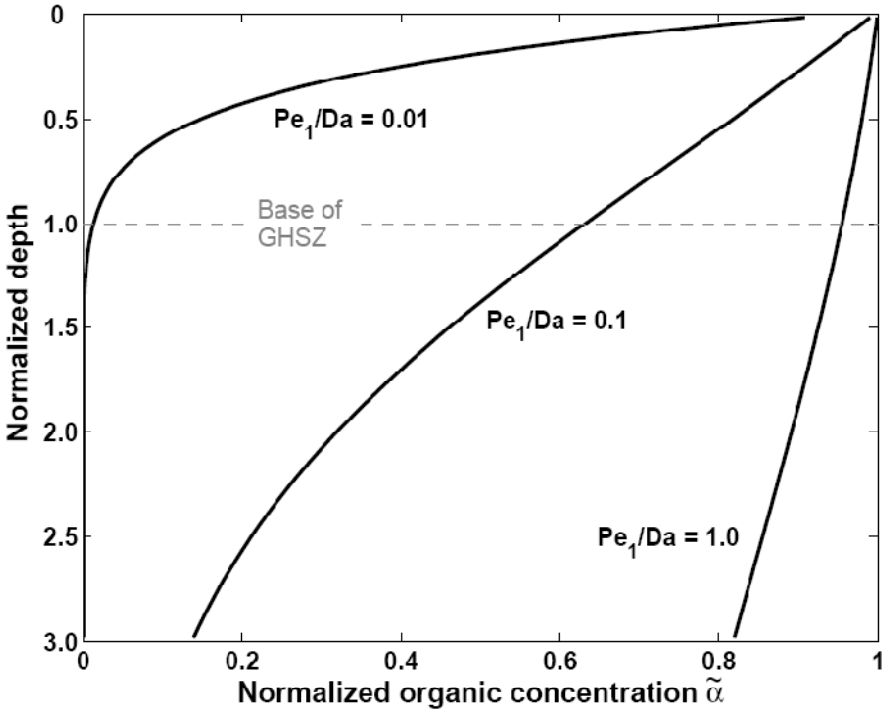

Figure 6.1.2: Normalized organic concentration profiles at steady state as a function of the ratio Pe1/Da (From Bhatnagar, 2007).

By the time sediments reach the base of the GHSZ, there is no organic material left that could be responsible for methane generation below the GHSZ for lower values of Pe_1/Da (order of 10^{-2}). Larger values of Pe_1/Da (order of 10^{-1}) result in a considerable amount of organic material leaving the base of the GHSZ. This provides a methane source at depth that can charge water and migrate upwards within the high permeability conduit to generate higher saturations of methane. In all our following simulation results, Pe_1/Da=0.1, is used so as to have more organic content leaving the GHSZ for higher methane generation below the GHSZ. For 1-D systems, average gas hydrate saturation contours are shown as a function of Pe_1 and the net amount of

organic carbon converted within the GHSZ (Bhatnagar et al., 2007). Steady state analytical solution of the organic mass balance is used to compute the normalized organic content at the base of the GHSZ (Bhatnagar, 2007) by the equation below.

$$\tilde{\alpha}|_{\tilde{z}=1} = [\eta + (1-\eta)e^{N_{t\phi}}]^{\frac{-1}{N_{t\phi}(1+\gamma)Pe_1/Da}}$$

Organic carbon converted within GHSZ is $= (1 - \tilde{\alpha}|_{\tilde{z}=1})\beta$

For the transport parameters defined above, organic carbon converted within GHSZ is 2.5.

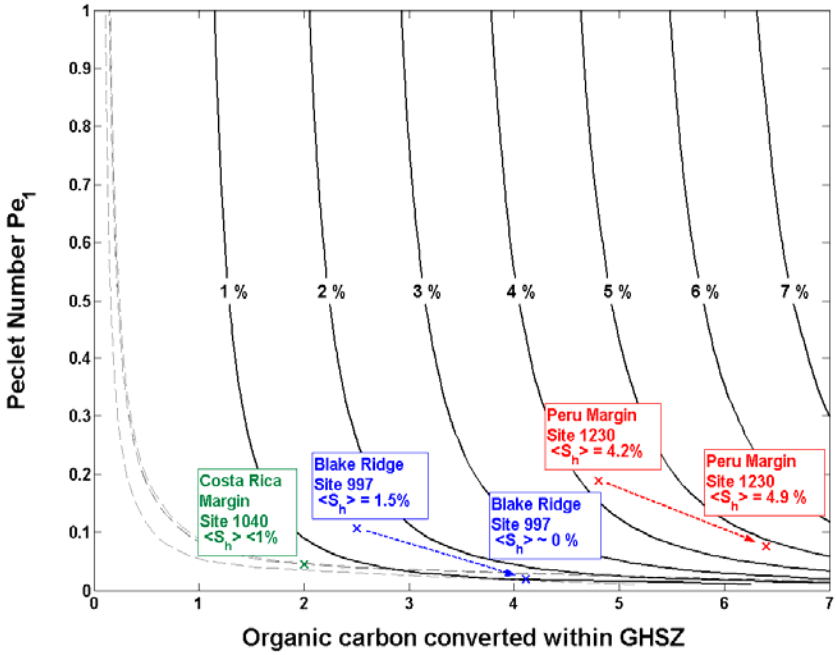

Figure 6.1.3: Gas hydrate saturation contours averaged over the entire GHSZ for systems where all methane is furnished through in situ biogenic reactions. Diffusive losses dominate at low values of Peclet number (Pe_1), implying that methane generation within the GHSZ has to increase to form any gas hydrate. The set of dashed curves, marked (a) and (b), represent the intermediate region of gas hydrate formation without free gas, with the region of no gas hydrate formation for x-axis values lesser than for curve (a) and gas hydrate with free gas immediately below for x-axis values greater than those for curve (b). Average gas hydrate saturation at different gas hydrate settings can be obtained from this single contour map. (From Bhatnagar *et al*., 2007)

For corresponding values of $Pe_1 = 0.1$ and organic carbon converted, average hydrate saturation is ~1.5% corresponding to the Blake Ridge region.

Results at different transient states are presented as follows. The first simulation run was with homogeneous sediment permeability to replicate the 1-D results previously published (Bhatnagar *et al*., 2007). Gas hydrate and free gas saturation contours are shown in Figure 6.1.4.

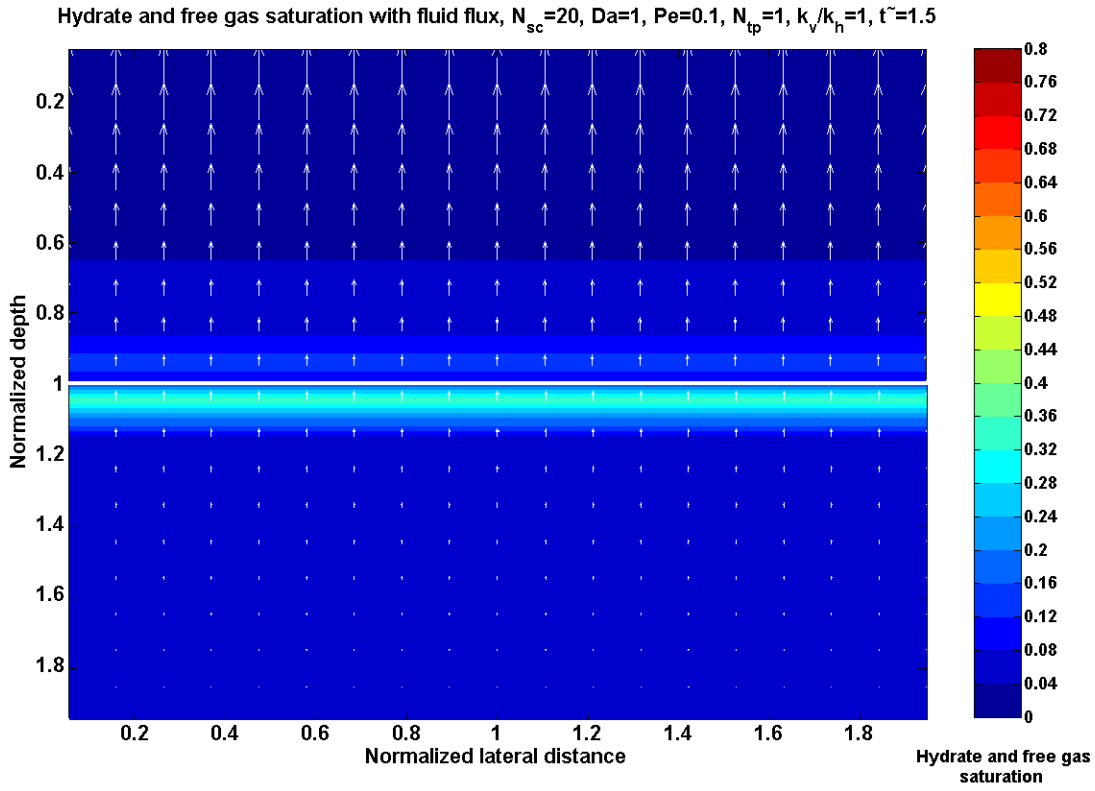

Figure 6.1.4: Gas hydrate and free gas saturation contours at dimensionless time $\tilde{t} = 1.5$ for a homogeneous, isotropic system. Parameters: N_{sc} =20, k_v/k_h =1, Da=1, Pe_1/Da=0.1, $N_{t\varphi}$=1

Average hydrate saturation for isotropic, homogeneous case is 1.6% with peak hydrate saturation 16% and peak gas saturation 36% matches very well with the 1-D results discussed above in figure 6.1.3. The physical domain of normalized depth for all the simulations is $\tilde{z} \in [0,2]$ and the normalized lateral distance $\tilde{x} \in [0,2]$. Normalized depth and lateral distance are scaled by characteristic depth to the base of the GHSZ as defined as follows.

$$\tilde{z} = \frac{z}{L_t} \qquad\qquad \tilde{x} = \frac{x}{L_t}$$

The arrows represent net fluid flux flowing in the upward direction relative to sedimentation scaled to maximum flux values. The broad white line at normalized depth $\tilde{z} = 1$ represents the BHSZ. The color bars represent gas hydrate and free gas saturations. Due to the laterally uniform deposition of the sediments, hydrate and free gas saturation also remain constant across the lateral direction. Thus, this system is essentially 1-D in nature. Since the lateral ends of the domain are no-flow boundaries, there is no lateral fluid flow in this system. Consequently, there is no fluid focusing or enhanced concentration of hydrate or free gas within the sediments. To introduce lateral heterogeneities in the system, we will now simulate examples of fracture systems and dipping sand layers.

Fracture system is now introduced and the transient gas hydrate and free gas accumulation are followed through time. Simulations with a vertical fracture network, 100 times more permeable than the surrounding formation that extends through the gas hydrate stability zone (GHSZ) up to the seafloor show focused fluid flow causing relatively higher hydrate and free gas saturation within the fracture network compared to the surrounding, lower permeability formation. The location of the fracture system in all the subsequent contour plots is shown by the set of dashed lines. The effect of the fracture system in focusing flow along this high permeability conduit is clearly observed through the enhanced hydrate saturations within the fracture system. The focused fluid flow is visualized by vector field plots and helps us to understand higher saturations of hydrate in these fracture systems. Simulation results at different normalized time are reported in figures 6.1.5 through 6.1.8. To understand the anisotropy in realistic geologic settings, anisotropic results with varying ratio of vertical permeability to horizontal permeability (k_v/k_h) in the surrounding clay sediments are discussed in the following section. Table 6.1.1 is included to illustrate all the simulation cases along with the parameters discussed.

Table 6.1.1: Illustrates various cases along with the simulation parameters that were varied to explain the results below.

Figure	**Cases**	**N_{sc}**	**k_v/k_h**	**Da**	**Pe_1/Da**	**Time**	***$N_{t\varphi}$***
6.1.4	Homogeneous system	20	1	1	0.1	1.5	1
6.1.5	Vertical fracture system	20	1	1	0.1	0.6	1
6.1.6	Vertical fracture system	20	1	1	0.1	1.5	1
6.1.7	Vertical fracture system	20	10^{-2}	1	0.1	1.5	1
6.1.9	Dipping sand layer system	20	10^{-2}	1	0.1	1.0	1
6.1.10	Dipping sand layer system	20	10^{-2}	1	0.1	1.5	1

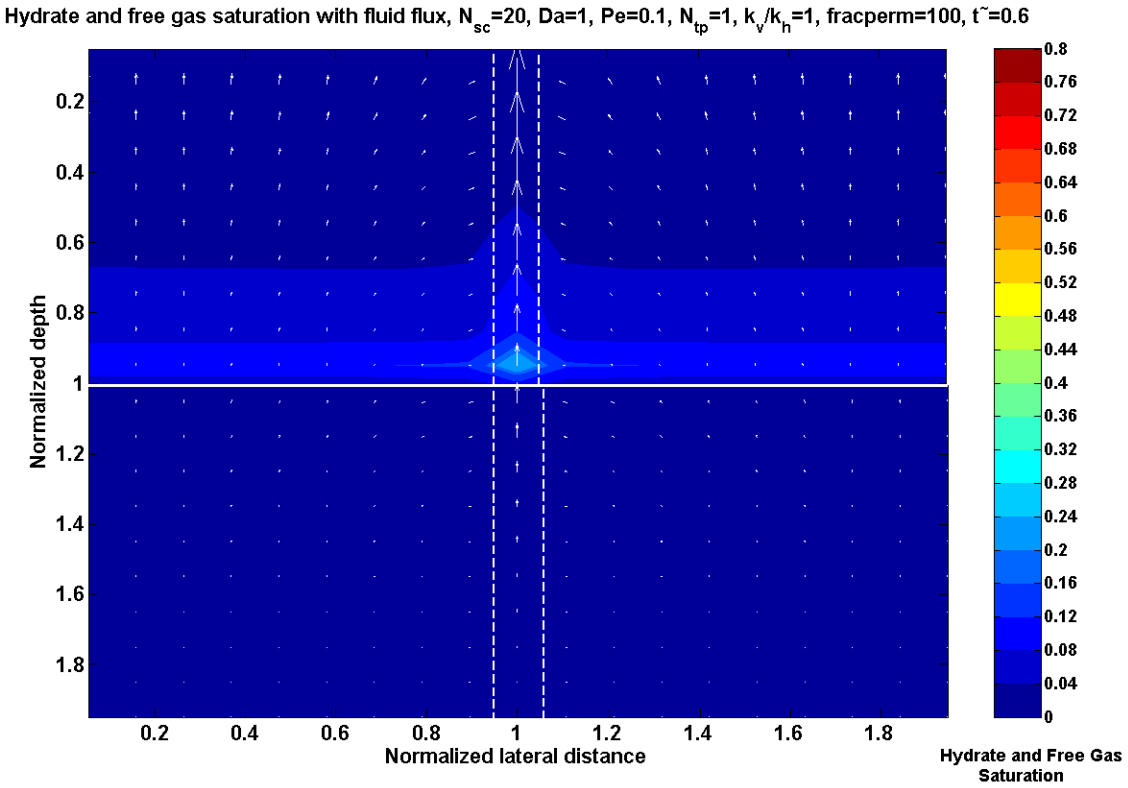

Figure 6.1.5: Gas hydrate and free gas saturation contours at dimensionless time t=0.6 for a vertical fracture system. Parameters: N_{sc} =20, k_v/k_h =1, Da=1, Pe_1/Da=0.1, $N_{t\varphi}$=1

In an isotropic system, with vertical fractures, peak gas hydrate saturation within the fracture system is about 24%, while peak hydrate saturation in the surrounding sediments is about 13% at time $\tilde{t} = 0.6$ (Figure 6.1.5). Free gas saturation at time $\tilde{t} = 0.6$, shown in figure 6.1.5 also depicts maximum gas saturation along the fracture column. However, free gas saturation at this time is low enough to not cause any lateral migration. Figure 6.1.6 shows gas hydrate saturation contours at a longer time $\tilde{t} = 1.5$.

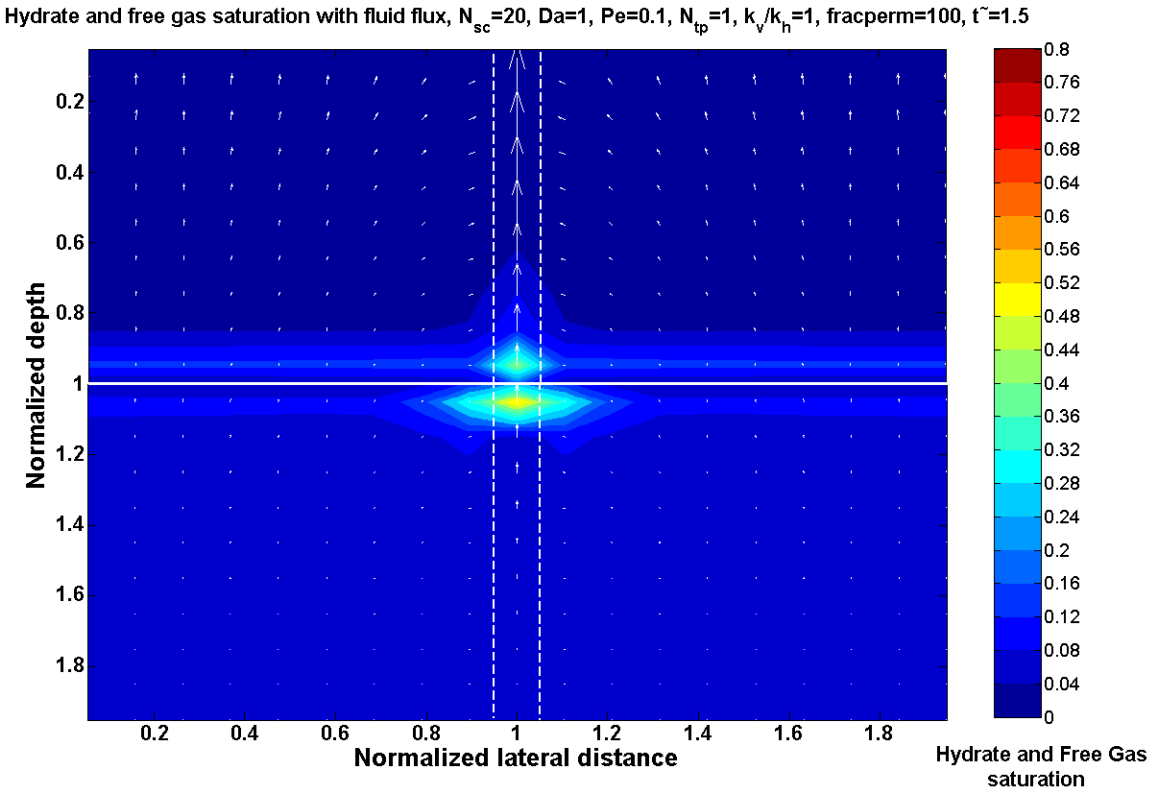

Figure 6.1.6: Gas hydrate and free gas saturation contours at dimensionless time t=1.5 for a vertical fracture system. Parameters: N_{sc} =20, k_v/k_h =1, Da=1, Pe_1/Da=0.1, $N_{t\varphi}$=1

Compared to Figure 6.1.5, peak hydrate saturation increases to 42% and occurs within the fracture system just above the base of the GHSZ. This peak value is more than twice the peak hydrate saturation (17%) in the surrounding sediments at the base of the GHSZ. Figure 6.1.6 also shows free gas saturation contours at $\tilde{t} = 1.5$. Buoyant free gas migrates upwards and gets sealed by the low permeability hydrate layer at the base of the GHSZ. Maximum free gas saturation (54%) occurs just below the GHSZ along the high permeability fracture system. At this enhanced saturation, free gas is mobile and migrates laterally, causing neighboring grid blocks just below the GHSZ to also have relatively higher saturations. Finally, gas hydrate saturation results are reported at time $\tilde{t} = 1.5$ in Figure 6.1.7, for anisotropic cases. On varying the ratio k_v/k_h to (order 10^{-2}), peak hydrate saturation is observed to be about 49% within the fracture system and is large as compared to 15% saturation in the sediment formation close to the base of the GHSZ.

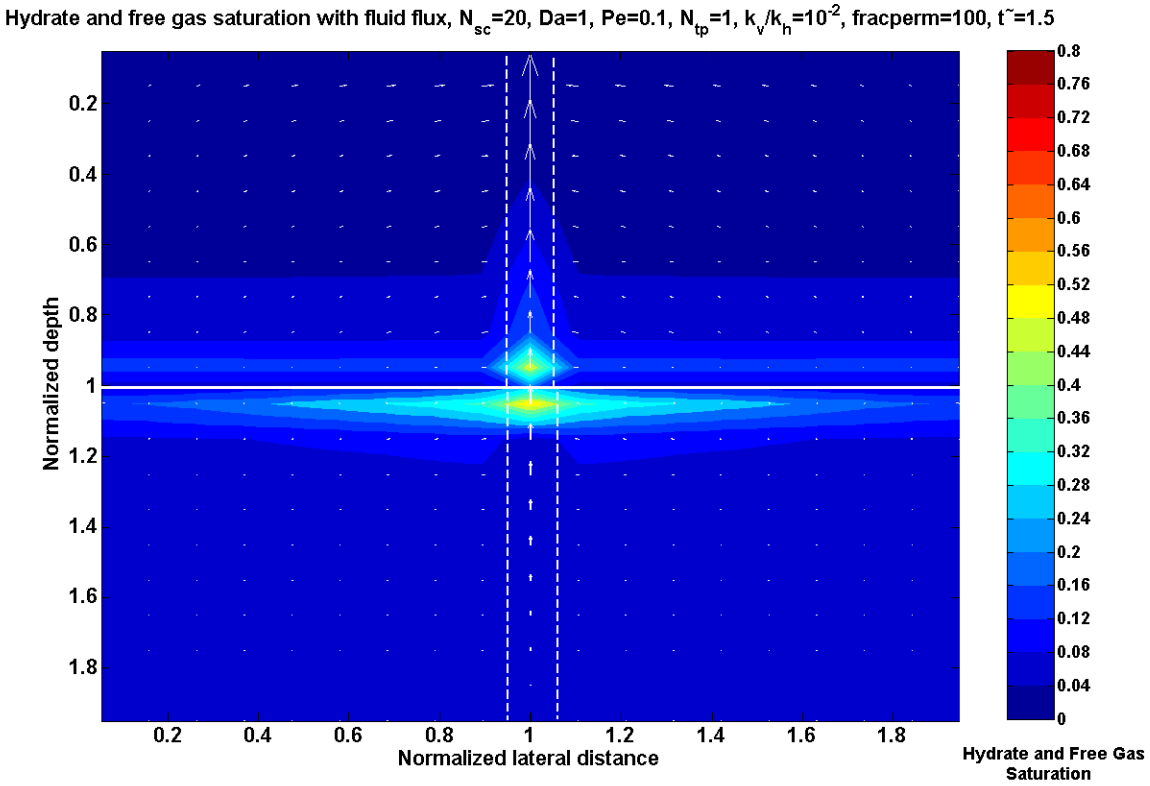

Figure 6.1.7: Gas hydrate and free gas saturation contours at dimensionless time $\tilde{t} = 1.5$ for a vertical fracture system with anisotropy. Parameters: N_{sc} =20, k_v/k_h =10^{-2}, Da=1, Pe_1/Da=0.1, $N_{t\varphi}$=1

Anisotropic cases with lower ratio of k_v/k_h (order 10^{-2}) show relatively higher hydrate saturations within the fracture network system because anisotropy focuses more of the fluid into the high permeability conduit. The flow is more prominent with lower realistic values of k_v/k_h. Free gas saturation below the GHSZ at $\tilde{t} = 1.5$ (Figure 6.1.7) increases to a peak value of about 58% within the fracture and spreads out laterally away from the fracture.

This section summarizes our findings that the presence of vertical fracture systems with higher permeability significantly affects gas, hydrate and free gas distribution by focusing fluid flow along these fracture systems. Higher hydrate and free gas saturations are observed in the higher permeability fracture systems as a result of the increased fluid flux.

Gas Hydrate Systems with Dipping Sand Layers

In addition to vertical fracture systems, our model also incorporates stratigraphy of varying permeabilities, to simulate dipping sand layers between low permeability shaley layers. To model a dipping sand layer, our simulator includes a pre-existing sand layer at a given angle within the sediment formation between two low permeability shaley layers which is allowed to deposit and be buried with passage of time. High

permeability sand layers extend up to the end of the simulation domain. The downward movement of this sand layer and the corresponding transient hydrate/free gas evolution are then recorded through time. Similar to the fracture network case, high permeability is assigned to different grid blocks at a particular angle as shown in the figure below. The initial permeability schematic illustrated in Figure 6.1.8 shows the initial location of this high permeability sand layer.

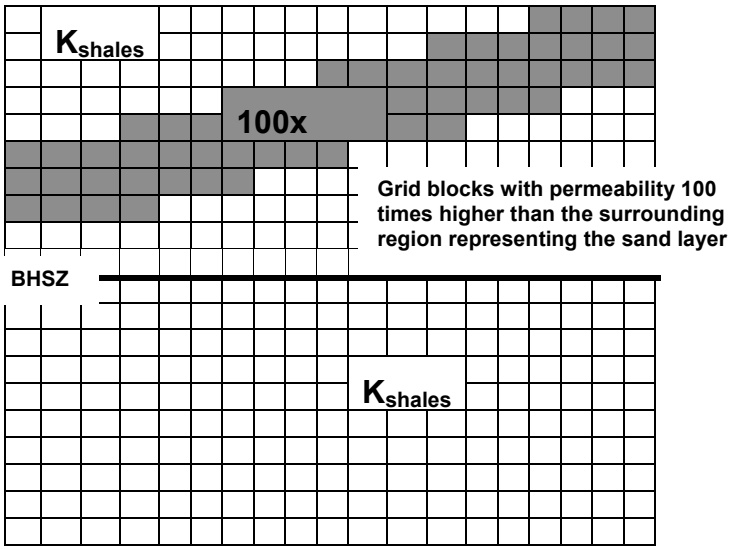

Figure 6.1.8: The initial permeability schematic representing initial high permeability sand layers with permeability 100 times greater than the surrounding shaley sediments

The sand layer is assigned an absolute permeability 100 times greater than the surrounding shaley formation. The physical domain of normalized depth for all the simulations is $\tilde{z} \in [0,2]$ and normalized lateral distance $\tilde{x} \in [0,10]$. The critical gas saturation is assumed to have value of 5%. The dimensionless transport parameters are $Pe_1 = 0.1,\ Da = 1,\ \beta = 6,\ \gamma = 9,\ \eta = 6/9,$ and $N_{t\phi} = 1$. Seafloor conditions and other parameters pertaining to relative permeabilities, capillary pressure, and physical properties of water, hydrate and gas remain the same as in section 6.1. Systems with dipping sand layers show similar localized, enhanced concentrations of hydrate and free gas within the high permeability conduits. Gas hydrate and free gas saturation contours are shown in figure 6.1.9 and 6.1.10 for two different times $\tilde{t} = 1.0$ and $\tilde{t} = 1.5$. The plots show significant higher hydrate saturation within the sand layer. The focused fluid flow in high permeability sand layer is evident from the results shown. Free gas is also focused within the sand layer. Fluid flux is shown using vector plots along with saturation contour maps to help us to understand higher saturations in the high permeability sand layers. A set of dashed lines shows position of the sand layer within the low permeability shaley matrix. The arrows represent net fluid flux flowing in the upward direction relative to sedimentation scaled to maximum flux values. The broad white line at normalized depth $\tilde{z} = 1$ represents the BHSZ. The color bars represent gas hydrate and free gas saturations.

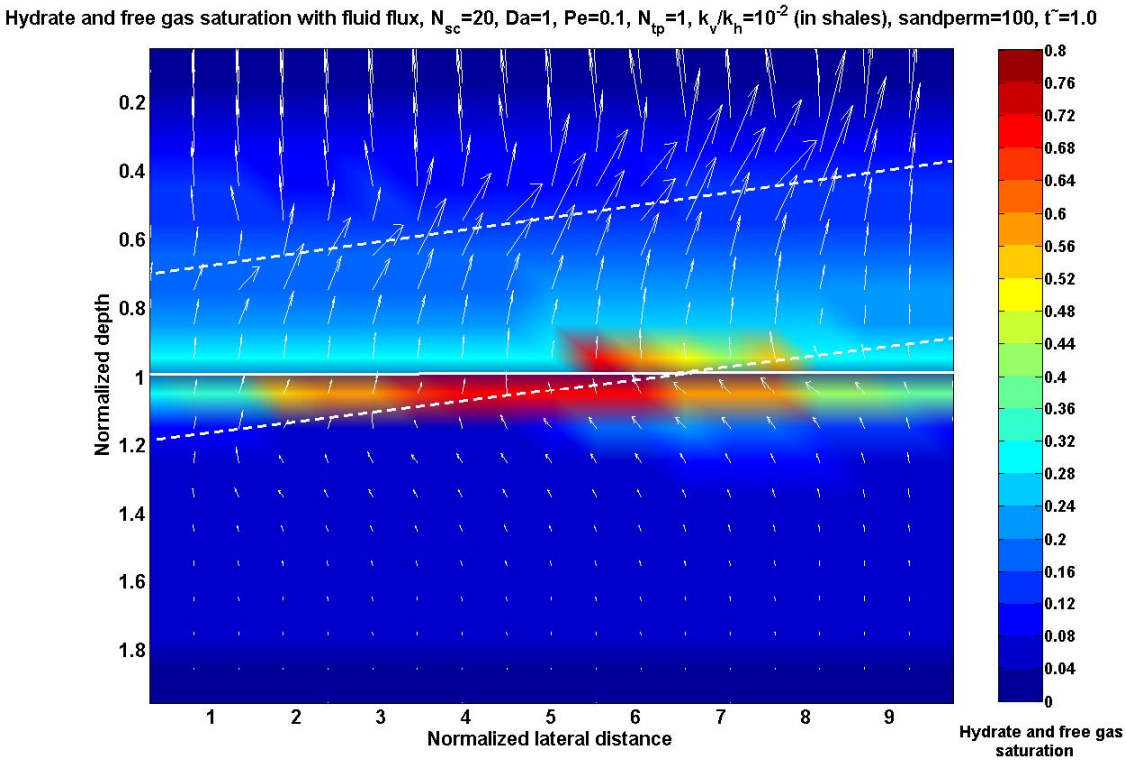

Figure 6.1.9: Gas hydrate and free gas saturation contours at normalized time $\tilde{t} = 1.0$ for dipping sand layers. Parameters: N_{sc}=20, $k_v/k_h=10^{-2}$(in shales), Da=1, Pe_1=0. 1

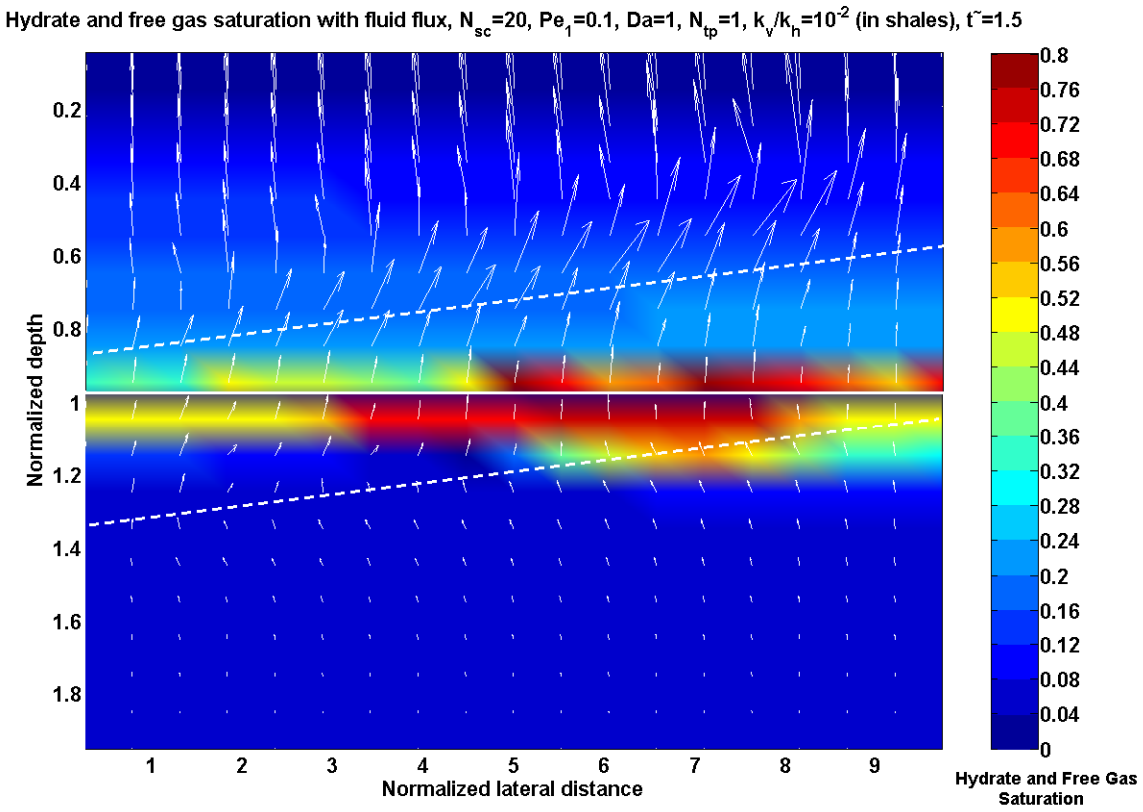

Figure 6.1.10: Gas hydrate and free gas saturation contours at normalized time $\tilde{t} = 1.5$ for dipping sand layers. Parameters: N_{sc}=20, $k_v/k_h=10^{-2}$(in shales), Da=1, Pe_1=0. 1

At $\tilde{t} = 1.5$ (Figure 6.1.10) peak hydrate saturation within the sand layer is about 80%, significantly higher than the 20% peak hydrate saturation in the low permeability sediments within the GHSZ. Free gas saturation is about 75% within the sand layer just below the GHSZ and, similar to all previous figures, free gas spreads laterally into the low permeability sediments outside the sand layer. Thus, keeping all other parameters the same, the higher permeability sand layer leads to relatively higher fluid focusing and hydrate saturation within the GHSZ. The simulation results presented above elucidate that lithology plays a significant role in producing heterogeneous gas hydrate and free gas accumulations.

Conclusions and Future Work

A dimensionless, two-dimensional (2-D) model was developed in this chapter to simulate gas hydrate and free gas accumulation in marine sediments over geologic timescales. Development of a 2-D model allows incorporation of lithologic heterogeneity and lateral fluid flow in the system. Focused fluid flow through a vertical fracture network and/or high permeability sand layers affecting regional and local hydrate accumulation and saturation can be elucidated with the help of this 2-D model. Currently, relatively simple systems with fracture systems and/or dipping sand layers are simulated, whereas realistic geologic settings are characterized by much more heterogeneous stratigraphy in terms of fracture networks, multiple sand layers embedded within shaley layers and combination of fracture systems and sand layers.

These preliminary results, however, serve as a starting point and demonstrate that the numerical model can be used to simulate systems with considerable heterogeneity to realize the natural gas hydrate systems more precisely.

References

Bhatnagar G., PhD. Thesis (2008), Accumulation of gas hydrates in marine sediments, Rice University, p 192-236

Bhatnagar, G., Chapman, W.G., Dickens, G.R., Dugan, B. and Hirasaki, G.J. (2007), Generalization of gas hydrate distribution and saturation in marine sediments by scaling of thermodynamic and transport processes, *Am. J. Sci.*, 307: p 861-900

Weinberger, J. L. and Brown, K. M. (2006), Fracture networks and hydrate distribution at Hydrate Ridge, Oregon. *Earth Planet. Sci. Lett*., 245(1):123-136

Trehu, A. M., Long, P. E., Torres, M. E., Bohrmann, G., Rack, F. R., Collett, T. S., Goldberg, D. S., Milkov, A. V., Riedel, M., Schultheiss, P., Bangs, N. L., Barr, S. R., Borowski, W. S., Claypool, G. E., Delwiche, M. E., Dickens, G. R., Gracia, E., Guerin, G., Holland, M., Johnson, J. E., Lee, Y. J., Liu, C. S., Su, X., Teichert, B., Tomaru, H., Vanneste, M., Watanabe, M., and Weinberger, J. L. (2004), Three-dimensional distribution of gas hydrate beneath southern Hydrate Ridge: Constraints from ODP Leg 204. *Earth Planet. Sci. Lett.*, 222:845-862

Weinberger, J. L. and Brown, K. M. (2006), Fracture networks and hydrate distribution at Hydrate Ridge, Oregon. *Earth Planet. Sci. Lett*., 245(1):123-136

Subtask 6.8(b) Sulfate/ methane/ bicarbonate/ calcium profile as indicator of methane flux: Sayantan Chatterjee

The upward flux of methane is an important determinant for the amount of hydrate that may potentially be present in the sediments. One approach to measure methane flux is to relate sulfate methane transition (SMT) depth to the methane flux via anaerobic oxidation of methane (AOM). Dickens suggests that AOM is the most dominant reaction in natural gas hydrate systems. However, numerous prominent authors such as Kastner *et al*. argue that consumption of pore water sulfate in shallow sediments is a result of oxidation of particulate organic carbon (POC) and not methane (Kastner et al., 2008). The articles in *Fire in the Ice* by Kastner *et al*., 2008 and Dickens and Snyder, 2009 focus on these two important arguments in the gas hydrate community and warrant more detailed modeling to help resolve the questions raised by these prominent groups. Sulfate consumption has been observed to follow two reaction pathways in marine sediments. The two pathways are shown as below:

POC driven sulfate consumption $2CH_2O + SO_4^{2-} \rightarrow 2HCO_3^- + H_2S$

Anaerobic Oxidation of Methane (AOM) $CH_4 + SO_4^{2-} \rightarrow HCO_3^- + HS^- + H_2O$

Stoichiometry and Dominant Reaction for Sulfate Consumption

Anaerobic Oxidation of Methane

Dickens suggests that methane is responsible for the sulfate consumption at the SMT via AOM. The AOM reaction involves oxidation of one mole of methane and subsequent reduction of one mole of sulfate to sulfide forming one mole of bicarbonate (Borowski et al. 1999).

$$CH_4 + SO_4^{2-} \rightarrow HCO_3^- + HS^- + H_2O$$

The AOM reaction takes place at the sulfate methane transition (SMT) zone and is characterized by near-zero depleted pore water concentrations of methane and sulfate. The sulfate concentration profile increases upwards towards the seafloor, and the methane concentration profile increases downwards away from the seafloor. Dickens suggests that AOM dominates the consumption of pore water sulfate by a 1:1 stoichiometry as shown above.

Particulate Organic Carbon (POC) driven sulfate consumption

Kastner argues that the dominant reaction is the particulate organic carbon (POC) driven sulfate consumption. She suggests that POC reacts with one mole of sulfate, reduces it to sulfide and forms two moles of bicarbonate maintaining the stoichiometric ratio as 2:1.

$$2CH_2O + SO_4^{2-} \rightarrow 2HCO_3^- + H_2S$$

Since the above reaction is independent of methane, upward methane fluxes cannot be determined using pore water sulfate profiles and therefore she suggests that SMT depth cannot be an indicator of methane flux. Kastner shows a cross plot of change in excess alkalinity versus change in pore water sulfate concentration for shallow sediments. Excess alkalinity is the amount of HCO_3^- that would occur in pore water if carbonate had not precipitated. The change in excess alkalinity can be computed by summing the deviations in pore water alkalinity, Ca^{2+} and Mg^{2+} relative to their respective concentration in seawater. The change in pore water sulfate concentration is also relative to the seawater. The cross plot shows a 2:1 slope which might suggest that one mole sulfate releases two moles of bicarbonate and supports POC driven sulfate consumption (Kastner *et al*., 2008). This conclusion would be valid if she would assume a closed system where zero flux comes in or goes out of the system. Kastner reported change of pore water sulfate and bicarbonate concentrations relative to seawater only above the SMT, neglecting their respective fluxes.

Dickens *et al*., suggest that species flux analysis would be a better representation to understand the stoichiometry of the sulfate consumption reaction. Dickens and Snyder suggest that a sulfate and bicarbonate flux comparison study is more logical than the concentration comparison since pore water sulfate and bicarbonate species would diffuse in opposite directions above the SMT. Dickens and Snyder calculate sulfate and bicarbonate fluxes across the SMT from ODP leg 1244 data as shown in figure 6.8.1. They calculated that -6 mol/m^2-kyr of HCO_3^- enters the SMT from below due to deeper bicarbonate flux and -22 mol/m^2-kyr of HCO_3^- leave the SMT towards the seafloor allowing a net change of -16 mol/m^2-kyr of HCO_3^- across the SMT towards the seafloor. The negative sign is due to the flux measurement in the

upward direction of depth. They also show a net +16 mol/m^2-kyr of SO_4^{2-} change from above the SMT due to the sulfate consumption in the downward direction of depth (Dickens and Snyder, 2009).

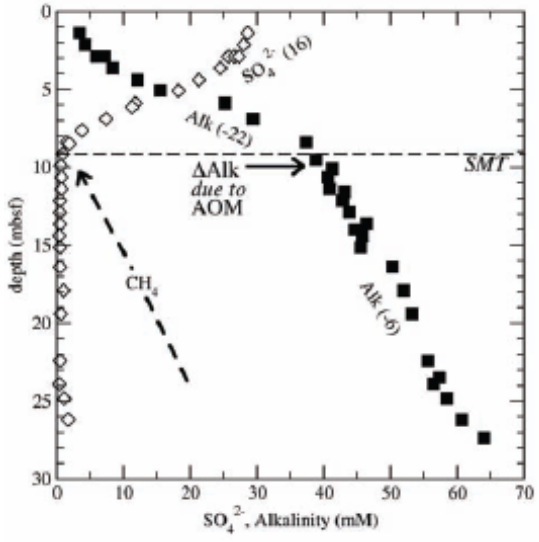

Figure 6.8.1: Pore water data in shallow sediment at ODP 1244, hydrate ridge (Trehu et al., 2003). Also shown are the SMT, estimated fluxes of dissolved species (mol/m^2-kyr) in and out of the SMT (Dickens and Snyder, Winter 2009)

The flux analysis by Dickens *et al*., accounts for the deep flux of HCO_3^- with carbonate correction. This analysis is in contrast to the analysis of departure of concentration values from the seafloor as suggested by Kastner *et al*. The computed fluxes are reported and seen to have a 1:1 ratio between HCO_3^- and SO_4^{2-} fluxes, which justifies AOM as being the dominant reaction for sulfate consumption. Following flux estimation in figure 6.8.1 shown above, a simple bicarbonate mass balance can be written as shown in the equation below:

$$HCO_{3\ deep}^- + HCO_{3\ AOM}^- = HCO_{3\ shallow}^- - HCO_{3\ CO_3^{2-}\_correction}^-$$

where $HCO_{3\ deep}^-$ is the bicarbonate due to the deep flux of bicarbonate coming from lower sediments towards the seafloor, $HCO_{3\ AOM}^-$ is the bicarbonate emanating from the AOM reaction at the SMT, $HCO_{3\ shallow}^-$ is due to the shallow flux of bicarbonate going upwards towards the seafloor and $HCO_{3\ CO_3^{2-}\_correction}^-$ is the bicarbonate which results in authigenic carbonate precipitation with divalent ions like Calcium.

The source of deep flux of bicarbonate is essentially the biogenic generation of methane. The methanogenesis reaction involves biogenic breakdown of two moles of organic carbon solids to form one mole of methane and one mole of carbon dioxide which reacts with pore water to form bicarbonate via a series of reactions as shown:

$$\textit{Fermentation}:$$
$$6CH_2O + 2H_2O \rightarrow 2CH_3COOH + 2CO_2 + 4H_2$$
$$\textit{Methanogenesis}:$$
$$CO_2 + 4H_2 \rightarrow CH_4 + 2H_2O$$
$$2CH_3COOH \rightarrow 2CH_4 + 2CO_2$$
$$\overline{\textit{Overall}: 2CH_2O \rightarrow CH_4 + CO_2}$$

$$CO_2 + OH^- \rightarrow HCO_3^-$$

Over geologic timescales, sedimentation and deposition of older sediments buries the organic carbon to greater depths. This gives rise to the deeper bicarbonate flux coming from below.

Carbon isotopic composition $\delta^{13}C$ in Dissolved Inorganic Carbon (DIC)

The second argument proposed by Kastner *et al*., is based on the carbon isotopic composition ($\delta^{13}C$) of dissolved inorganic carbon (DIC) across the SMT. Dissolved inorganic carbon (DIC) is essentially bicarbonate and is often referred to as DIC by Kastner in her results. The different reactions along with their respective isotopic carbon composition ($\delta^{13}C$) values are shown below.

The organic carbon is depleted in $\delta^{13}C$ depleted (-25‰). Two molecules of organic carbon form one molecule each of methane and carbon dioxide. The

biogenic methane is depleted in $\delta^{13}C$ (-60‰) and carbon dioxide is rich in $\delta^{13}C$ (+10‰). Carbon dioxide eventually forms bicarbonate with water and gets buried with time and results in deep bicarbonate flux with $\delta^{13}C$ (+10‰).

Methanogenesis reaction: $2CH_2O + OH^- \rightarrow CH_4 + HCO_3^-$

-25‰ -60‰ +10‰

POC driven sulfate consumption $2CH_2O + SO_4^{2-} \rightarrow 2HCO_3^- + H_2S$

-25‰ -25‰

AOM reaction at the SMT $CH_4 + SO_4^{2-} \rightarrow HCO_3^- + HS^- + H_2O$

-60‰ -60‰

Carbon isotopic composition ($\delta^{13}C$) of bicarbonate is (-60‰) in the AOM reaction and is (-25‰) in the POC reaction. Kastner points out that the $\delta^{13}C$ of bicarbonate across the SMT is considerably greater when methane is the source of sulfate reduction instead of POC (Kastner et al., 2008). However, in their analysis, system is closed and all fluxes are neglected. The deep bicarbonate flux which is rich in $\delta^{13}C$ is not accounted when they evaluate the $\delta^{13}C$ composition in bicarbonate.

In contrast Dickens justifies that the measured values of $\delta^{13}C$ in bicarbonate (-25‰) above the SMT is balanced by the net flux of methane (-60‰) and deep flux of bicarbonate (+10‰) coming from below. Dickens suggests that deep bicarbonate flux is an important term to be included in $\delta^{13}C$ balance calculations.

Proposed work

We have to examine both the hypotheses by these two prominent groups using Bhatnagar's 1-D model. Bhatnagar's current 1-D model computes mass balances with both advective and diffusive fluxes. We believe that sulfate consumption reaction following both the pathways (i.e: POC driven and anaerobic oxidation of methane) should be included in the current model. Setting the model parameters to represent zero flux, and thus assuming a closed system, we should be able to show Kastner's results. Bicarbonate and Ca^{2+} profiles can be computed in addition to the sulfate and methane profiles along depth. Our existing 1-D model already computes the methane and sulfate profiles, but an additional bicarbonate and Ca^{2+} mass balance (for calculating carbonate precipitation) would provide a complete understanding of the deep bicarbonate flux. This deep flux of bicarbonate profile would validate Dickens' results and justify the dominance of the AOM reaction for consumption of sulfate in shallow sediments. Remodeling our current 1-D model is pertinent, so we propose to indicate methane flux with the help of pore water sulfate profiles along with bicarbonate (alkalinity) balance as a tool to investigate both the hypotheses claimed by these two prominent groups.

Numerical Model including both Reaction Pathways for Sulfate Consumption

Following Bhatnagar's one-dimensional model (Bhatnagar, 2007) methane mass balance equations has been simplified to exclude hydrate and free gas phase terms. The following equation includes water phase methane balance only. It also assumes both methane generation from particulate organic carbon (POC) and consumption via anaerobic oxidation of methane (AOM) reactions in the balance equation.

Methane Mass Balance

$$\frac{\partial}{\partial t}(\phi S_w \rho_w c_m^l) + \frac{\partial}{\partial z}(U_f \rho_w c_m^l) = \frac{\partial}{\partial z}(\phi \rho_w S_w D_m \frac{\partial c_m^l}{\partial z}) + \frac{M_{CH_4}}{M_{org}} \rho_{sed}(1-\phi)\lambda\alpha$$

$$- \frac{\phi S_w \lambda_{AOM}(\rho_w c_m^l)(\rho_w c_s^l)}{M_{SO_4}}$$

The sulfate mass balance is in the water phase only and it includes both the reaction pathways for sulfate consumption. The anaerobic oxidation of methane and particulate organic carbon both act as sinks for pore water sulfate and both these reactions are included in our proposed model.

Sulfate Mass Balance

$$\frac{\partial}{\partial t}(\phi S_w \rho_w c_s^l) + \frac{\partial}{\partial z}(U_f \rho_w c_s^l) = \frac{\partial}{\partial z}(\phi \rho_w S_w D_s \frac{\partial c_s^l}{\partial z}) - \frac{M_{SO_4}}{M_{org}} \rho_{sed}(1-\phi)\lambda\alpha$$

$$- \frac{\phi S_w \lambda_{AOM}(\rho_w c_m^l)(\rho_w c_s^l)}{M_{CH_4}}$$

As pointed out in an earlier section, bicarbonate balance is a necessary step to examine the two hypotheses claimed by the two groups. Similar to the sulfate balance, bicarbonate mass balance includes source terms originating from both the reactions discussed above. The bicarbonate mass balance is in the water phase like the sulfate balance and is presented below.

Bicarbonate Mass Balance

$$\frac{\partial}{\partial t}(\phi S_w \rho_w c_b^l) + \frac{\partial}{\partial z}(U_f \rho_w c_b^l) = \frac{\partial}{\partial z}(\phi \rho_w S_w D_b \frac{\partial c_b^l}{\partial z}) + \frac{2M_{HCO_3}}{M_{org}} \rho_{sed}(1-\phi)\lambda\alpha$$

$$+ \frac{M_{HCO_3}\phi S_w \lambda_{AOM}(\rho_w c_m^l)(\rho_w c_s^l)}{M_{CH_4} M_{SO_4}}$$

The above equations can be non-dimensionalized using the scaling scheme developed by Bhatnagar *et al*., (2007). The dimensionless mass balance equations are presented as follows.

Dimensionless Methane Balance

$$\frac{\partial}{\partial \tilde{t}}\left[\frac{(1+\gamma\tilde{\phi})S_w \tilde{c}_m^l}{\gamma}\right] + \frac{1+\gamma}{\gamma}\frac{\partial}{\partial \tilde{z}}\left[\left(Pe_1 + Pe_2 - \frac{Pe_1 \tilde{U}_{sed}(1+\gamma\tilde{\phi})S_h c_w^h \tilde{\rho}_h}{\gamma(1-\tilde{\phi})}\right)\tilde{c}_m^l\right]$$

$$= \frac{\partial}{\partial \tilde{z}}\left[\frac{(1+\gamma\tilde{\phi})S_w}{\gamma}\frac{\partial \tilde{c}_m^l}{\partial \tilde{z}}\right] + \frac{M_{CH_4}}{M_{org}}\tilde{\rho}_{sed} Da(1-\tilde{\phi})\tilde{\alpha}\beta$$

$$- \frac{(1+\gamma\tilde{\phi})S_w}{\gamma}\frac{M_{CH_4} c_{s,o}}{M_{SO_4} c_{m,eqb}^l} Da_{AOM} \tilde{c}_m^l \tilde{c}_s^l$$

Dimensionless Sulfate Balance

$$\frac{\partial}{\partial \tilde{t}}\left[\frac{(1+\gamma\tilde{\phi})S_w \tilde{c}_s^l}{\gamma}\right] + \frac{1+\gamma}{\gamma}\frac{\partial}{\partial \tilde{z}}\left[\left(Pe_1 + Pe_2 - \frac{Pe_1 \tilde{U}_{sed}(1+\gamma\tilde{\phi})S_h c_w^h \tilde{\rho}_h}{\gamma(1-\tilde{\phi})}\right)\tilde{c}_s^l\right]$$

$$= \frac{\partial}{\partial \tilde{z}}\left[\frac{(1+\gamma\tilde{\phi})S_w}{\gamma}\frac{D_s}{D_m}\frac{\partial \tilde{c}_s^l}{\partial \tilde{z}}\right] - \frac{M_{SO_4}\tilde{c}_{m,eqb}}{M_{org} c_{s,o}}\tilde{\rho}_{sed} Da(1-\tilde{\phi})\tilde{\alpha}\beta - \frac{(1+\gamma\tilde{\phi})S_w Da_{AOM}\tilde{c}_m^l \tilde{c}_s^l}{\gamma}$$

Dimensionless Bicarbonate Balance

$$\frac{\partial}{\partial \tilde{t}}\left[\frac{(1+\gamma\tilde{\phi})S_w\tilde{c}_b^l}{\gamma}\right]+\frac{1+\gamma}{\gamma}\frac{\partial}{\partial \tilde{z}}\left[\left(Pe_1+Pe_2-\frac{Pe_1\tilde{U}_{sed}(1+\gamma\tilde{\phi})S_h c_w^h\tilde{\rho}_h}{\gamma(1-\tilde{\phi})}\right)\tilde{c}_b^l\right]$$

$$=\frac{\partial}{\partial \tilde{z}}\left[\frac{(1+\gamma\tilde{\phi})S_w}{\gamma}\frac{D_b}{D_m}\frac{\partial \tilde{c}_b^l}{\partial \tilde{z}}\right]+\frac{2M_{HCO_4}\tilde{c}_{m,eqb}}{M_{org}c_{b,o}}\tilde{\rho}_{sed}Da(1-\tilde{\phi})\tilde{\alpha}\beta$$

$$+\frac{1+\gamma\tilde{\phi}}{\gamma}\frac{M_{HCO_3}}{M_{SO_4}}\frac{S_w Da_{AOM}c_{s,o}\tilde{c}_m^l\tilde{c}_s^l}{c_{b,o}}$$

where S_i denotes saturation of phase i in the pore space, $\tilde{\rho}_i$ is the density of the phase i normalized by density of water, M_i is the molecular weight. Methane, sulfate and bicarbonate diffusivities are denoted as D_m, D_s, and D_b respectively. The subscripts w correspond to water, m to methane, s to sulfate, b to bicarbonate, and sed to sediment respectively. Superscript l corresponds to liquid water phase in all the equations. The vertical depth is normalized by the depth of base of the GHSZ $\tilde{z}=\frac{z}{L_t}$. Time is normalized by a combination of depth of the BSHZ L_t and methane diffusivity D_m as $\tilde{t}=\frac{t}{{L_t}^2/D_m}$. Methane mass fraction in phase i is normalized by methane solubility in the liquid phase at the base of GHSZ $c_{m,eqb}$, while sulfate and bicarbonate mass fractions are normalized by their respective seawater values $c_{s,o}$ and $c_{b,o}$ to get their corresponding normalized variables. The normalized variables are defined as:

$$\tilde{c}_m^l=\frac{c_m^l}{c_{m,eq}^l} \qquad \tilde{c}_s^l=\frac{c_s^l}{c_{s,o}^l} \qquad \tilde{c}_b^l=\frac{c_b^l}{c_{b,o}^l}$$

The reduces porosities, $\tilde{\phi}$, $\tilde{\eta}$ and $\tilde{\gamma}$, normalized sediment flux $\tilde{U}_{sed}$, are defined as:

$$\gamma=\frac{1-\phi_\infty}{\phi_\infty} \qquad \eta=\frac{\phi_0-\phi_\infty}{1-\phi_\infty} \qquad \tilde{\phi}=\frac{\phi-\phi_\infty}{1-\phi_\infty} \qquad \tilde{U}_{sed}=\frac{U_{sed}}{U_{f,sed}}$$

where ϕ is the porosity of sediments, ϕ_o is the initial porosity at the seafloor, ϕ_∞ is the minimum porosity attained at greatest depth, and $U_{f,sed}$ is the fluid flux due to sedimentation and compaction. The fluid flux $U_{f,sed}$ can be defined as a combination of seafloor sedimentation rate $\dot{S}$ and porosities.

$$U_{f,sed}=\frac{1-\phi_o}{1-\phi_\infty}\dot{S}\phi_\infty$$

The Peclet numbers Pe_1, Pe_2 and the two Damkohler numbers Da, Da_{AOM} have been defined as:

$$Pe_1 = \frac{U_{f,sed}\, L_t}{D_m} \qquad Pe_2 = \frac{U_{f,ext}\, L_t}{D_m}$$

$$Da = \frac{\lambda L_t^2}{D_m} \qquad Da_{AOM} = \frac{\rho_w c_{m,eqb}}{M_{CH_4}} \frac{\lambda_{AOM} L_t^2}{D_m}$$

where $U_{f,ext}$ is the fluid flux due to external sources from deeper sediments, λ is first order reaction rate for the methanogenesis reaction and λ_{AOM} is the second order reaction rate for the AOM reaction. The initial and boundary conditions are given as follows.

Initial conditions:

$\tilde{c}_m^l(\tilde{z},0) = \tilde{c}_s^l(\tilde{z},0) = \tilde{c}_b^l(\tilde{z},0) = 0$

Boundary conditions:

$\tilde{c}_m^l(0,\tilde{t})$=0 (Seafloor conditions)

$\tilde{c}_s^l(0,\tilde{t})$=1 (Seafloor conditions)

$\tilde{c}_b^l(0,\tilde{t})$=1 (Seafloor conditions)

$\tilde{c}_m^l(D_z,\tilde{t})$=$\tilde{c}_{m,ext}^l$

$\frac{\partial \tilde{c}_s^l}{\partial \tilde{z}}(D_z,\tilde{t}) = 0$

$\frac{\partial \tilde{c}_b^l}{\partial \tilde{z}}(D_z,\tilde{t}) = 0$

where $\tilde{c}_{m,ext}^l$ is the specified external concentration of methane at the bottom of the domain D_z

References:

Dickens, G.R., Snyder, G. (2009), Interpreting upward methane flux, Fire in the Ice, Winter, p 7-10

Kastner, M., Torres, M., Solomon, E., and Spivack, A. J. (2008), Marine pore fluid profiles of dissolved sulfate: do they reflect in situ methane fluxes? Fire in the ice, Summer, p 6-8

Borowski, W. S., Paull, C. K., and Ussler III, W. (1999) Global and local variations of interstitial sulfate gradients in deep-water, continental margin sediments: Sensitivity to underlying methane and gas hydrates. *Mar. Geol.*, 159:131–154

***Subtask 6.3. Compositional Effect on BSR:* Guangsheng Gu**

We show some evidence from literature about existence of multiple gas components in hydrate samples, and some well logging data which shows the existence of sII hydrate existing below the traditional Base of sI hydrate Stability Zone. And also we show the synthetic seismic response from a CH_4-C_3H_8-H_2O hydrate system, demonstrating the possibility of a weak BSR.

The presence of methane hydrate is usually detected by a bottom simulating reflector (BSR). The BSR results from the sudden change in acoustic impedance as the formation changes from being hydrate saturated to free-gas saturated at the base of the hydrate stability zone. If other hydrocarbons in addition to methane are present, this transition may take place over a depth greater than the acoustic wavelength and the BSR may be attenuated or absent.

Natural gas from thermogenetic sources may contain many types of gas components. Thus compositional effect should be considered when thermogenetic natural gas is present. Table 6.3-1 and Figure 6.3-1 show the existence of mixed hydrate in actual sites. Especially Figure 6.3-1 indicates the extending of hydrate below the base of pure methane hydrate (i.e., sI hydrate) stability zone.

Table 6.3-1. Existence of Multi-gas-component in Hydrate Samples

Unit of composition: mol %

Type	C_1	C_2	C_3	C_4*	CO_2	$C_1/(C_2+C_3)$
Biogenic (Garden Banks - 388, GOM)	**99.5**	**0.12**			**0.26**	**829**
(Orca Basin, GOM)	**99.1**	**0.34**	**0.28**		**0.24**	**159**
Thermogenic (Green Canyon - 234, GOM)	**74.3**	**4.0**	**13.0**	**4.06**	**4.6**	**4.4**
(Elm- Caspian Sea)	**81.4**	**15.3**	**1.6**	**0.9**	**0.8**	**4.81**

(D. Sloan, C. Koh, Clathrate Hydrate of Natural Gases, 3rd Ed., pp. 555.)

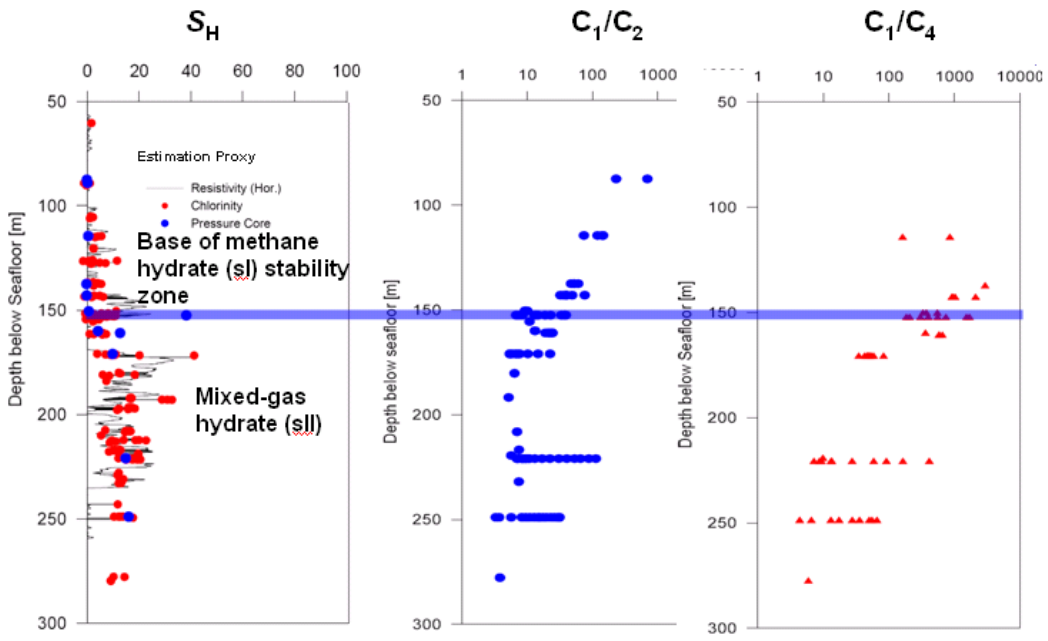

Figure 6.3-1. Evidence of Hydrate extending below pure CH_4 hydrate stability zone. (Gumusut-Kakap field, continental slope offshore Sabah, Malaysia; C. Hadley, *et al*., 2008, *International Petroleum Technology Conf.*, 12554.) C_1/C_2 indicates the ratio of CH_4 to C_2H_6.

In the following work, we focus on the CH_4-C_3H_8-H_2O hydrate system as an example. The effects of propane on the hydrate formation condition and on hydrate distribution, are studied. D. Sloan's CSMGem program is used to obtain the gas/liquid/hydrate equilibrium data.

An example saturation calculation will be presented in the end of the following work. The purpose of this example calculation is to demonstrate the possibility of gradual change of saturations with distance in sediment. The calculation is based on constant composition, whereas compositions will change during fluid migration in realistic cases.

Denote the overall molar fraction of species *i* as:

$$x_i = \frac{n_i}{n_{CH4} + n_{C3H8} + n_{H2O}}, \; i = CH_4, C_3H_8, H_2O.$$

where n_i is the amount of species *i* in the system (unit: mol), *i* = CH_4, C_3H_8, H_2O.

The water free molar fraction of species *i* is denoted as:

$$x_i^{wf} = \frac{n_i}{n_{CH4} + n_{C3H8}} = \frac{x_i}{x_{CH4} + x_{C3H8}}, \; i = C\,H_4, C_3H_8.$$

(1) Incipient Hydrate Formation Condition and Phase Regions

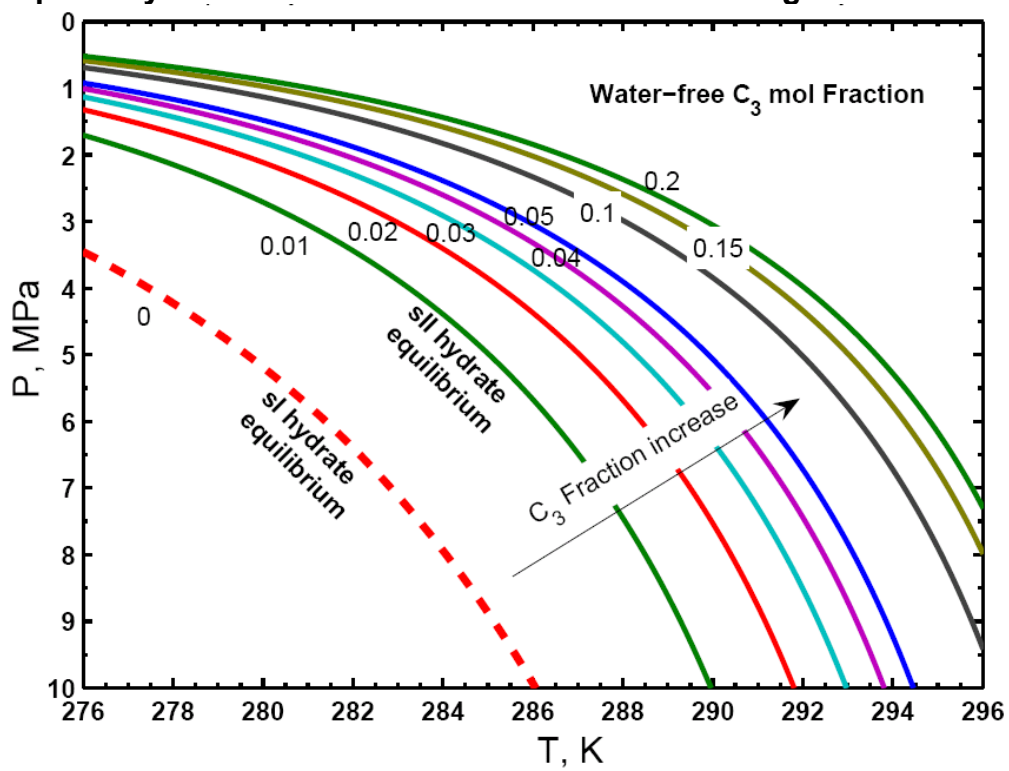

Fig. 6.3-2. Incipient Hydrate Formation Pressure of the CH_4-C_3H_8-H_2O System. Water is in excess. The data labeled for each curve, are the water-free propane molar fractions. The red dash curve, is for the pure CH_4-H_2O system (i.e. water-free propane molar fraction = 0).

Fig. 6.3-2 shows the incipient hydrate formation pressure of the CH_4-C_3H_8-H_2O System. For x_{C3H8}^{wf} = 0.01, the incipient hydrate formation pressure differs very much from that for the pure CH_4 system (i.e., x_i^{wf} = 0).

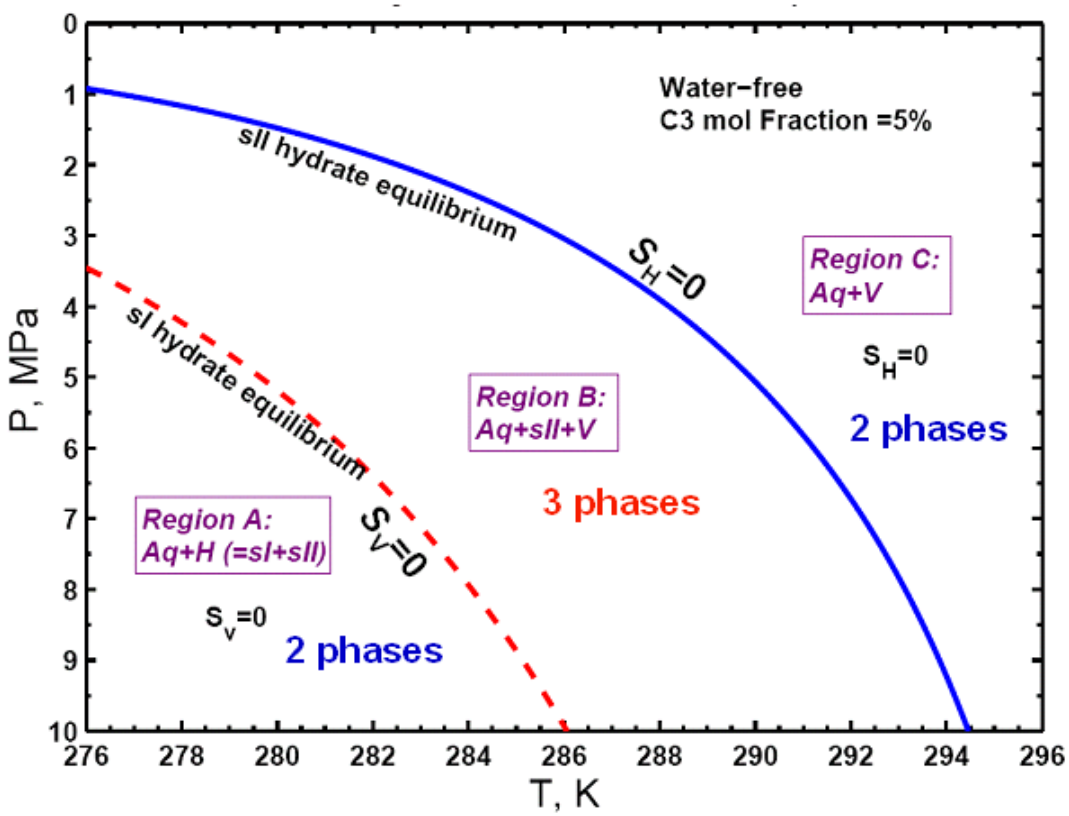

Fig. 6.3-3. Phase Regions of the CH_4-C_3H_8-H_2O System (water-free propane molar fraction is 0.05). Water is present in excess. The red dash curve is the incipient hydrate formation pressure for the pure CH_4-H_2O system. There are 3 regions: Region *A, B, C*. Region *A*: *Aq* + *Hydrate* (= *sI* + *sII*); Region *B*: *Aq* + *sII* + *V*; Region *C*: *Aq* + *V*. The red dash curve, and the blue solid curve, are boundaries for S_v=0 and S_H=0, respectively.

Fig. 6.3-3 presents the phase regions of the CH_4-C_3H_8-H_2O System (x_{C3H8}^{wf} is 0.05). 3 phase regions are marked in the figure. In Region A, both *s*I and *s*II hydrates are stable, while in Region B and C, sI is not stable. In Region B, sII is stable, while in Region C, sII hydrate is not stable. Therefore, in Region B, 3 phases can co-exist: Aq, H, and V. The boundaries for S_v=0 and S_H=0 are marked in the Fig. 6.3-3.

(2) Gradual Phase Transition (i.e. Saturation Change) in Sediment

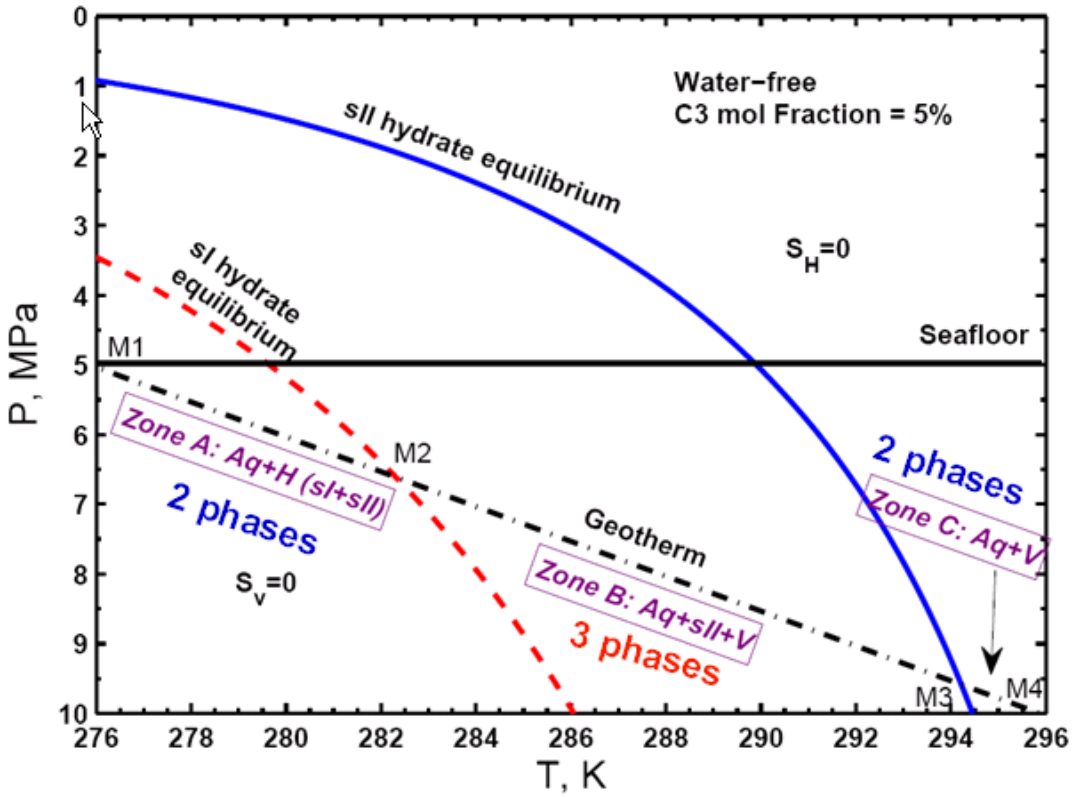

Fig. 6.3-4. Different zones of sediments of a CH_4-C_3H_8-H_2O System (water- free propane molar fraction is 0.05). The Geotherm curve is shown as the black dash-dot curve. There are 3 zones of sediments along the geotherm curve. Zone *A* (Line segment M_1M_2): *Aq + Hydrate* (= *sI + sII*); Zone *B* (Line segment M_2M_3): *Aq + sII + V*; Zone *C* (Line segment M_3M_4): *Aq + V*. Points M_2 and M_3, are boundaries for S_v=0 and S_H=0 in the sediment, respectively.

In Fig. 6.3-4 an example geotherm curve in sediment is considered. Three different zones may exist in the sediment along the geotherm curve, due to the 3 different phase regions described in Fig. 6.3-4. Zone *B* is a special: 3 phases, *Aq + H (sII) +V*, co-exist. The boundary for S_v=0 in the sediment is the point M_2 in Fig. 6.3-4, while that for S_H=0 is the point M_3. It's obvious that Zone B (Line segment M_2M_3) is a phase-transition-zone corresponding to the boundary of S_v=0 to that of S_H=0. Line segment M_2M_3 in Fig. 6.3-4, around 300 m in spatial distance, is definitely very long. Such a gradual change of saturations within a long distance, may result in gradual change of sediment acoustic properties, and further induce weak BSR or even absence of BSR. An example calculation can demonstrate the possibility of such kind of gradual saturation change, as shown in Fig 6.3-5.

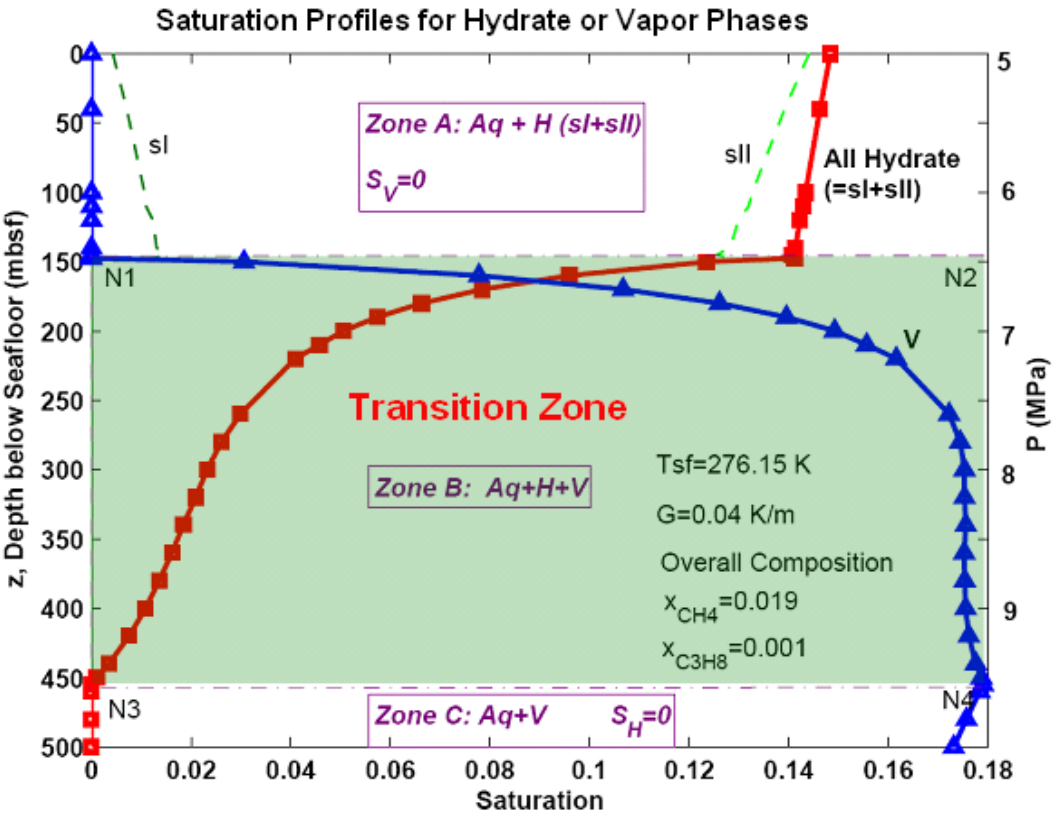

Fig. 6.3-5. An example calculation of a CH_4-C_3H_8-H_2O System (water-free propane molar fraction is 0.05; Overall composition x_{CH4}=0.019, x_{C3H8}=0.001, x_{H2O}=0.98). Assume: The overall composition is the same in the spatial domain. There are 3 zones of sediments in the domain. Zone A: *Aq + Hydrate* (= *sI + sII*); Zone B: *Aq + sII + V*; Zone C: *Aq + V*. Dash-dot line N_1N_2 and N_3N_4, are boundaries for S_v=0 and S_H=0 in the sediment, respectively. Red solid curve and blue solid curve are saturation profiles for All Hydrate (=sI + sII), and for Vapor, respectively. Seafloor temperature T_{sf} = 276.15 K. Geothermal gradient G= 0.04 K/m. Pressure is marked on the right side.

Fig. 6.3-5 is an example calculation of a CH_4-C_3H_8-H_2O System. The following conditions and assumptions are applied:

(1) Water-free propane molar fraction is 0.05 everywhere. (e.g., take overall composition x_{CH4}=0.019, x_{C3H8}=0.001, x_{H2O}=0.98.)
(2) Overall composition is constant in the spatial domain. Diffusion and convection has not been considered.
(3) Seafloor temperature T_{sf} = 276.15 K. Geothermal gradient G= 0.04 K/m.
(4) Seafloor Pressure P_{sf}=5 MPa.
(5) Porosity is the same everywhere, ϕ=0.2. Compaction has not been considered.

As is well known, there is a sharp phase transition in the CH_4-H_2O hydrate system, which is the basis for BSR. However, for a CH_4-C_3H_8-H_2O System, in Zone *B* in Fig. 6.3-5, from z=147.5 mbsf (Line N_1N_2) to z= 450 mbsf (Line N_3N_4), the S_H decreases continually from 14.1% to 0%, while S_V increases continuously

from 0% to 17.9%. Zone *B* is a phase transition zone, in which 3 phases (*Aq+H+V*) co-exist, and saturations change continuously.

A gradual saturation change will result in the gradual change of acoustic properties with increase in depth, and consequently, very possibly induce a weak BSR, or even absence of BSR.

Estimation of average velocity is via a revised form of the Time-average Equation (Pearson *et al.*, 1983).:

$$\frac{1}{V_p} = \frac{\phi(1 - S_H - S_V)}{V_w} + \frac{\phi S_H}{V_H} + \frac{(1-\phi)}{V_m} + \frac{\phi S_V}{V_V}$$

V_p --- average compressional velocity of the sediment;

V_H --- compressional velocity of the pure hydrate;

V_w --- compressional velocity of the fluid;

V_m --- compressional velocity of the mineral;

ϕ --- porosity (as a fraction);

S_H --- Hydrate saturation

S_V --- Vapor (Gas) saturation

Average density is estimated via:

$$\overline{\rho} = (1-\phi)\rho_m + \phi \sum_i S_i \rho_i$$

phase *i* =*w,H,V.*

Parameters used are in the Table 6.3-2:

Table 6.3-2. Parameters for Velocity and Density of Each Phase

Phase Component	**$V_{p,i}$ (m/s)**	**ρ_i (kg/m^3)**
Sea Water (*w*)	1500	1030
Hydrate (H)	3300	900
Mineral (m)	2000	2600
Vapor (V, average)*	~400	~ 50

* estimated from CSMGem v1.0 at the mid-point in the spatial domain.

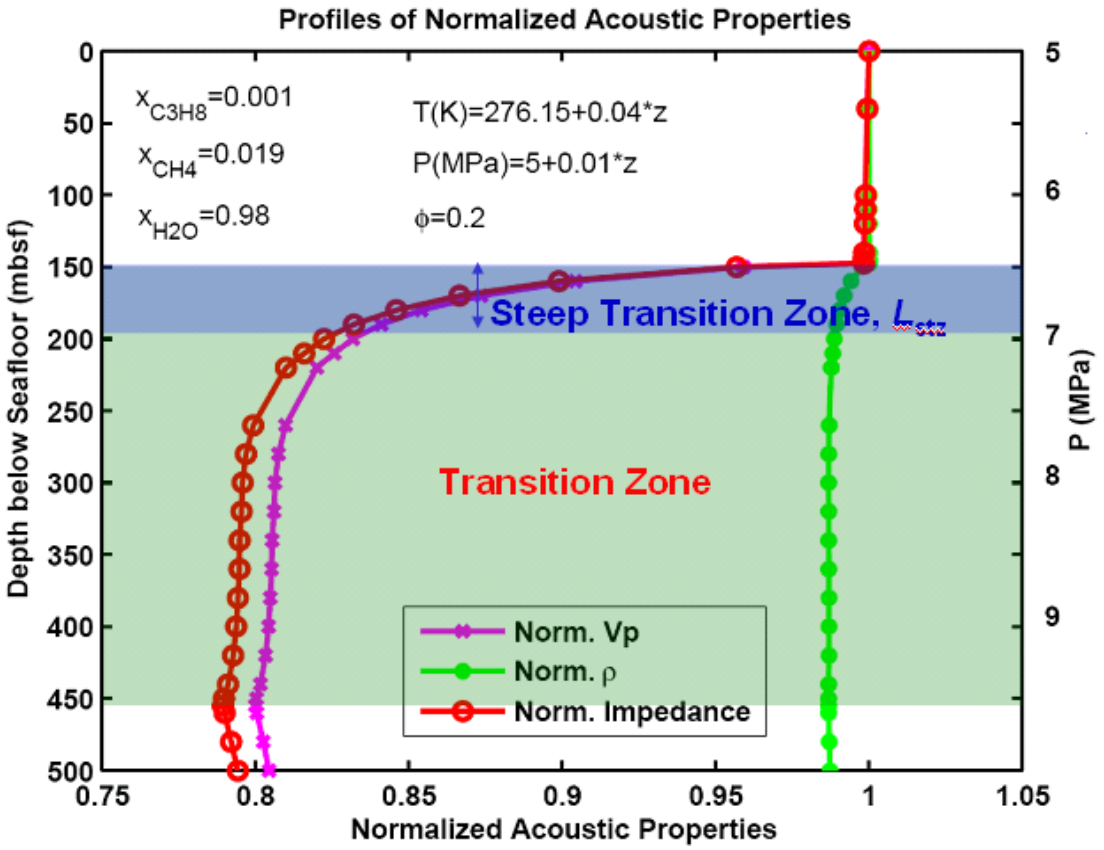

Fig. 6.3-6. Profiles of Normalized Acoustic Properties of the CH_4-C_3H_8-H_2O Hydrate System shown in Fig. 6.3-5. Impedance $Z = \rho V_p$. Data are normalized so that at seafloor the value is 1.

Figure 6.3-6 shows the estimated average p-wave velocity (normalized so that at seafloor the value is 1) and average density (normalized) of the system. We can find out that the density changes very slightly, within 2% from seafloor; the velocity varies much from seafloor to the bottom of the spatial domain. Therefore, the velocity variation is dominant. Figure 6.3-7 is a 2-D illustration of V_p distribution. In current stage, we haven't considered the compaction. In the future, we'll consider the compaction.

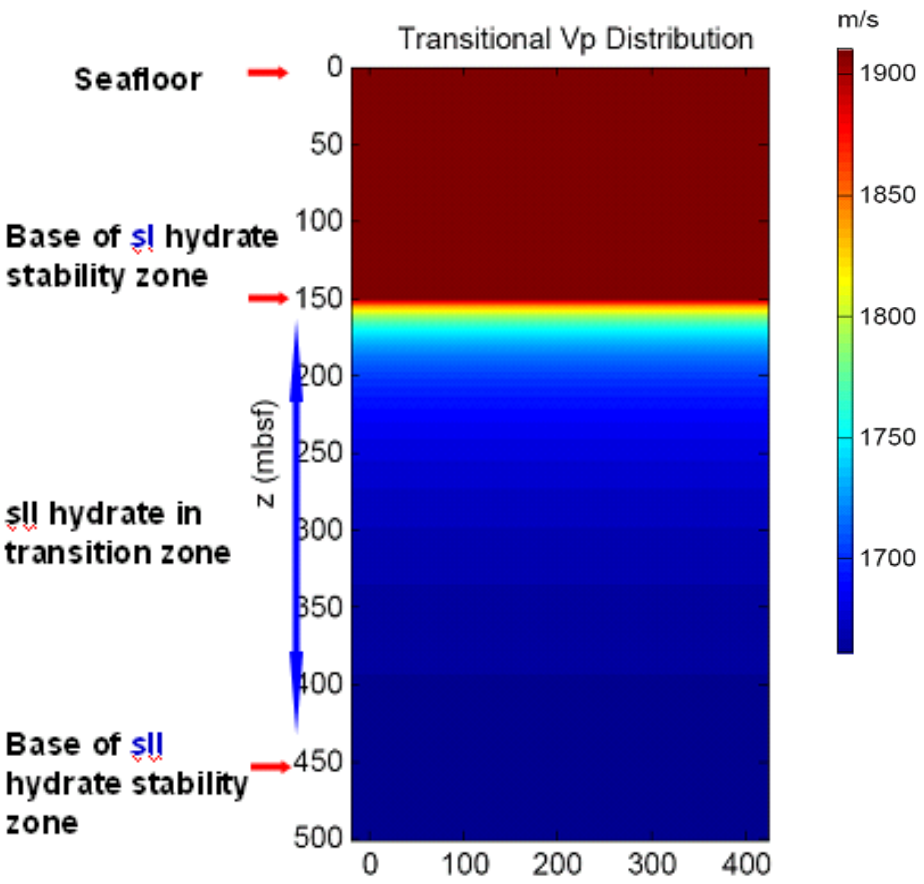

Figure 6.3-7. 2-D Illustration of the Transitional Vp Distribution in a CH_4-C_3H_8-H_2O Hydrate System. (Data are from Figure 6.3-6. Assume: (1) the same over-all composition everywhere in the spatial domain, (2) no lateral varitation, and (3) ϕ=0.2 everywhere.) Please notice the base of sI hydrate stability zone, and that of sII hydrate stability zone is different. Between these 2 bases, is the transition zone. This distribution will be used to evaluate the synthetic seismic response via a 2-D Waveform Inverse Code (Pratt, 1990) in the following figure.

Seismic Response:

As is well known, for a pure CH_4 hydrate system, due to an abrupt transition from hydrate layer to gas layer below (if gas layer exists closely to the base of GHSZ), a BSR is often expected, for whatever frequency often used in seismic detection. However, in a multiply gas component system shown in Figure 6.3-5, due to the thick transition zone, the seismic response is dependent on the frequency band we use.

1-D Seismic Model:

An 1-D seismic code, with 0 offset, is developed to test the seismic response from such a transition zone. The source signal is shown in Figure 6.3-8. From an abrupt change, the reflection will be very strong, as shown in Figure 6.3-9.

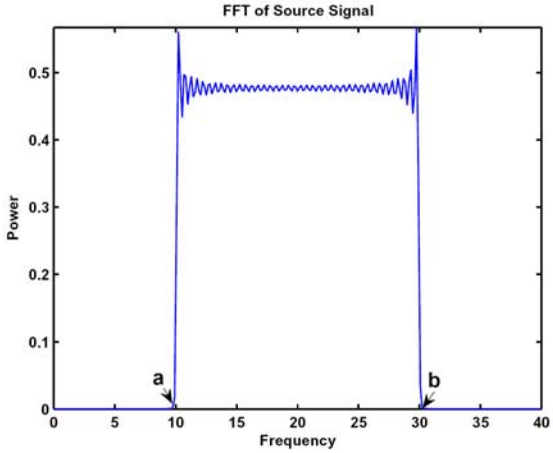

(a) Power Spectrum of Source Signal (Frequency band: 10~30 Hz, marked with a~b in the figure)

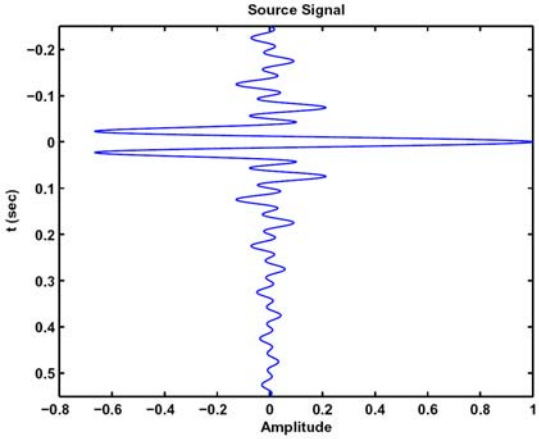

(b) Source Signal in Time Domain (Frequency band: 10~30 Hz)

Figure 6.3-8. Source Signal

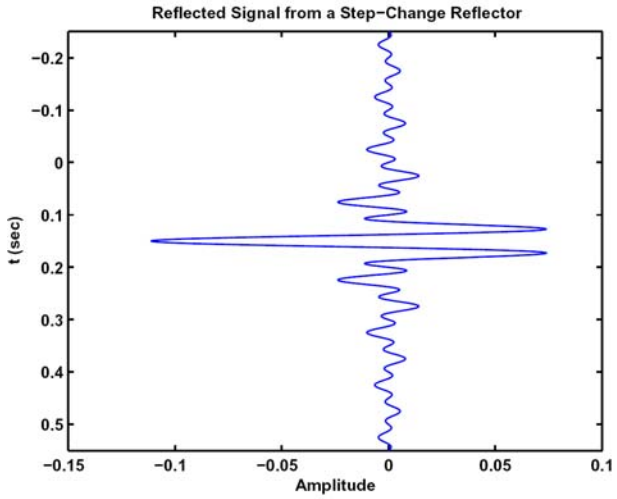

Figure 6.3-9. Seismic Reflection from an Abrupt Change of V_p Profile (i.e., a strong BSR). Frequency Band: 10~30 Hz. Please notice that the reflection is strong for whatever frequency band used.

However, for a transition zone, the reflection is dependent on the ratio of Characteristic Wavelength λ_c to Steep Transition Zone Thickness L_{stz}, as shown in Figure 6.3-10. Our current results show that:

If $\lambda_d/L_{stz} < 1$, reflection is very weak (hard to observe);

If $5 < \lambda_d/L_{stz} < 1$, reflection is weak (though still observable);

If $\lambda_d/L_{stz} > 5$, reflection is strong (easily observable).

Here weak or not is defined whether the response is observable in synthetic seismic responses. It's dependent on the amplitude of reflection comparing with that of the source wave.

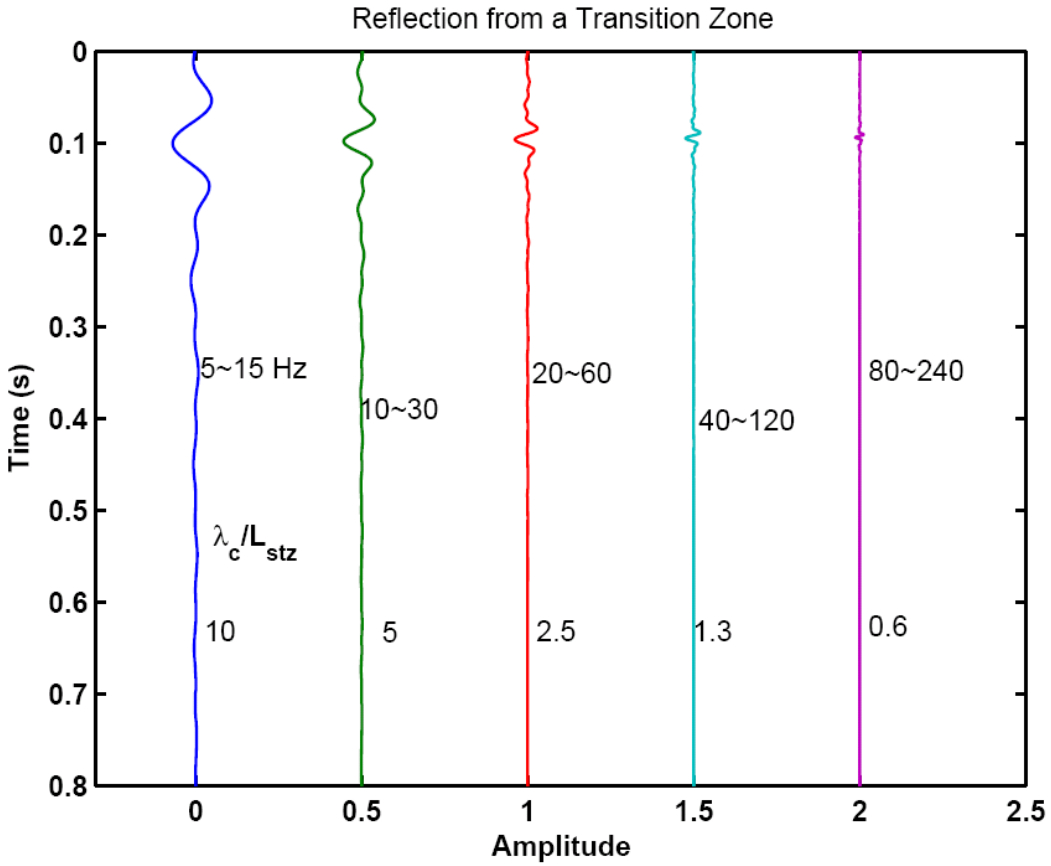

Figure 6.3-9. Reflection from a Transition Zone, by Using Different Frequency Bands

2-D Seismic Model:

Some synthetic seismic responses via a professional 2-D code are also generated to confirm the results in 1-D model above.

By using a 2-D Waveform Inverse Code (Pratt, 1990), the 2-D V_p distribution shown in Figure 6.3-7 applied, some synthetic seismic response are generated, as shown in Figure 6.3-10. The source wave is Ricker Wavelet with a central frequency f_c. For the Ricker Wavelet, characteristic wavelength λ_c is defined as the central wavelength. Central frequencies of 30 Hz and of 100Hz are tested in this 2-D code, respectively. In Figure 6.3-10, if the central frequency of the source wavelet is 100 Hz, then the reflection is very weak (hard to observe); if

the central frequency is 30 Hz, there is a weak (though still observable) BSR. This confirms the results via 1-D model.

In summary, the results indicates that, if λ_d/L_{stz} is too small, then we may not observe a strong BSR. In real cases, the L_{stz} may be even longer, then λ_d/L_{stz} may be too small to observe a strong BSR. This might be an explanation for many cases where hydrate exists but BSR is not observed.

Our results suggest that, for a multiple gas system, to detect BSR, it's better to use multiple frequencies, and most important, to use lower central frequencies.

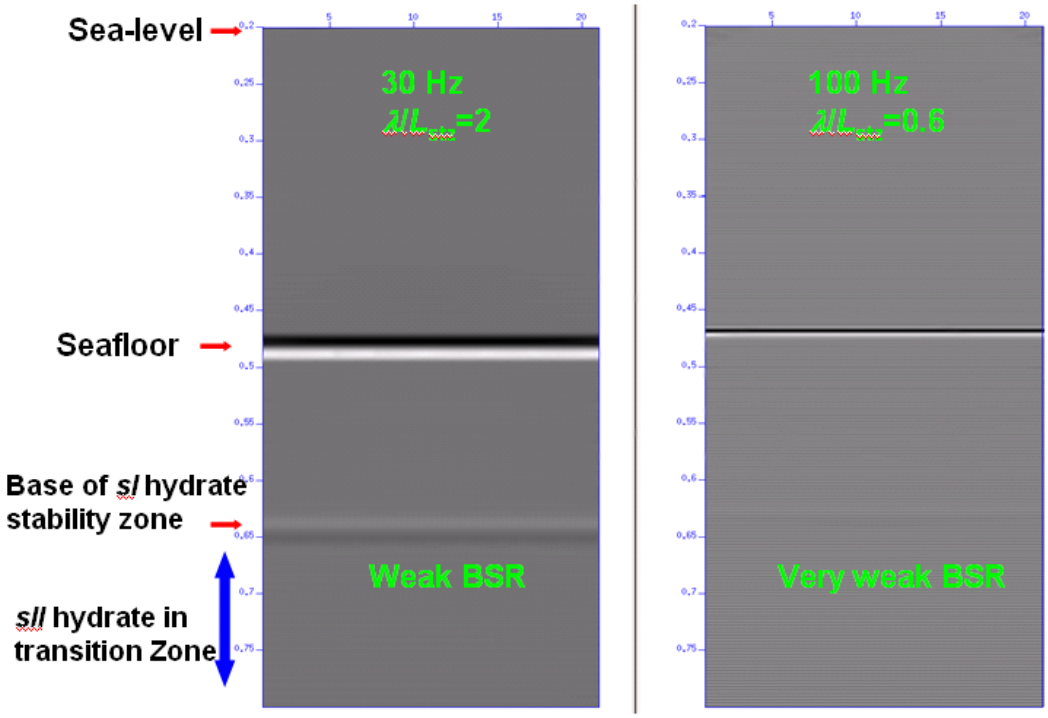

Fig. 6.3-10. Synthetic Seismic Response from the Transitional Vp Distribution. Code: 2-D Waveform Inverse Code (Pratt, 1990); Vp distribution is shown in Figure 6.3-7. Source wave signal is Ricker Wavelet with central frequency marked in the figure (30Hz and 100 Hz). The ratio λ/L_{stz} refers to the ratio of Central Wavelength to Steep Transition Zone Thickness.

Conclusion

(1) Existence of another gas component in marine hydrate system, can affect the hydrate and gas distribution greatly. As an example, for the CH_4-C_3H_8-H_2O hydrate system, due to different phase diagram from that of a pure CH4 hydrate system, 3 different phase regions are described for different *P-T* conditions. The transition region, Region B, is especially important, because Aq, H (sII), V can co-exist. Therefore, 3 zones can be present in the sediment. Zone B, is the

phase-transition-zone, because Aq, H (sII), V co-exist, and S_H and S_v change gradually.

(2) The result of an example saturation calculation of the CH_4-C_3H_8-H_2O hydrate system in the sediment is presented. It successfully demonstrated that gradual change of S_H and S_v over a long spatial distance (~300 m) is possible.

(3) Synthetic seismic responses are generated. Weak BSR or very weak BSR is possible if λ_d/L_{stz} <1. Our results suggest that, for a multiple gas system, it's better to use multiple frequencies to detect BSR, and most important, to use lower central frequencies than conventional frequencies used in seismic detection.

Task 7: Analysis of Production Strategy

J. Phirani & K. K. Mohanty, University of Houston

Abstract

Gas production from unconfined dipping class 2 hydrate reservoirs is studied. Depressurization alone is effective in dipping unconfined reservoirs, but gas production rate is much slower than that for warm water injection. As the injection point of the warm water moves down the reservoir, the start of the high gas recovery phase gets delayed, but the time for completion of gas recovery becomes shorter. The cost of wells and warm water must be optimized along with the gas production to determine the optimal strategy for producing hydrate reservoirs. We also presented a paper in the SPE Reservoir Symposium on history matching of core-scale hydrate formation and dissociation experiments.

Introduction

In our previous work, we had studied warm water flooding of horizontal unconfined class 2 hydrate reservoirs. For horizontal unconfined reservoirs, depressurization is ineffective; thermal stimulation is necessary for gas production. Even warm water (temperature ~ 30°C) injection improves the gas production from hydrate reservoirs. Lower vertical permeability helps the gas production by heating a larger area of the reservoir for hydrate dissociation. As the well spacing decreases, the gas production rate increases. In this work, gas production from unconfined dipping class 2 hydrate reservoirs is studied. We also presented a paper in the SPE Reservoir Symposium on history matching of core-scale hydrate formation and dissociation experiments.

Methodology

The objective of this study is to identify optimum production strategies for gas production from dipping unconfined Class 2 hydrate reservoirs through numerical simulation. For dipping reservoirs, 2-dimensional simulations are performed. A reservoir of 120m length, 10m thickness, and 18° dipping angle is assumed. The third dimension is assumed to be 120m to match the total volume to that of the horizontal reservoir. The volumes of hydrate and water layers in the dipping reservoir are kept the same as those in the horizontal reservoir. Initial temperature and pressure are assumed to be 7.5°C and 9MPa at the bottom of reservoir, respectively, which lie in the hydrate stable zone. The reservoir domain is discretized into 120 x 10 grid-blocks. Gas is lighter than the water; so the production well is placed at the top left corner. The depressurization pressure is 2MPa. Different positions of the injection well are considered, i.e., the middle of the reservoir (M) or the end of the reservoir (E). The injection pressure is 20MPa and the injection temperature is 30°C. To represent the semi-infinite aquifer at the bottom, the right most grid-block denoted by point ‘C’ in the Figure 1 is given a constant pressure. The water can flow through this boundary depending on the local pressure gradient. The other boundaries are considered

to be impermeable for mass flow and heat flow is represented with a heat transfer coefficient.

The numerical model used is a finite-volume simulator that takes into account heat transfer, multiphase fluid flow and equilibrium thermodynamics of hydrates. Four components (hydrate, methane, water and salt) and five phases (hydrate, gas, aqueous-phase, ice and salt precipitate) are considered in the simulator. Water freezing and ice melting are tracked with primary variable switch method (PVSM) by assuming equilibrium phase transition. Equilibrium simulation method is used here because kinetics of hydrate formation and dissociation are relatively fast in the field-scale. This in-house simulator has been validated in the DOE code comparison study.

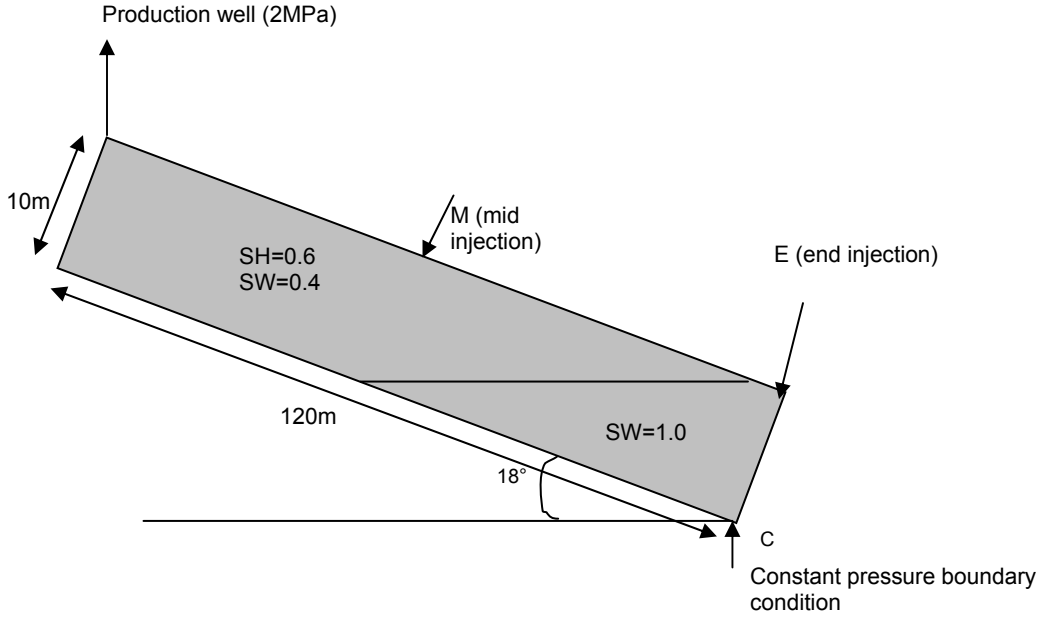

Figure 1: Schematic of an unconfined dipping reservoir

Results

Methane production was simulated for different injection pressures, injection temperatures and production pressures for 3000 days and total production of gas was compared for these parameters.

Figure 2 shows the cumulative gas production as a percentage of original gas in place for three different cases. The 'no injection' case stands for only depressurization. In the 'end injection' case warm water is injected at point E (in Figure 1) in the water layer. In the 'mid injection' case, warm water is injected at the point M (in Figure 1) in the middle of hydrate layer. The gas production is about the same for all the three cases in the 300 days; since the production is mainly due to depressurization at the production well. After that the mid injection gas production rate increases significantly, due to breakthrough of the warm water at the top part of the reservoir. The breakthrough of warm water in the end injection case happens a little later around 600 days and the gas production rate also increases sharply over that of the no injection case. All the hydrate is dissociated in 1000 to 1200 days for the warm water injection cases. It takes about 3000 days to produce 87% of the gas in the no injection case.

Gas production is slower, but effective in the no injection unconfined dipping reservoirs. This is because the semi-infinite aquifer is not very close to the production well, unlike that in the horizontal reservoir case. Figure 3 shows the hydrate saturation, aqueous saturation and the temperature profiles at 3000 days for the no injection case. Hydrate saturation profile shows that all the hydrates are not completely dissociated at 3000 days. Dissociation is slow because the latent heat comes from the surrounding medium, primarily through conduction. Temperatures are relatively low.

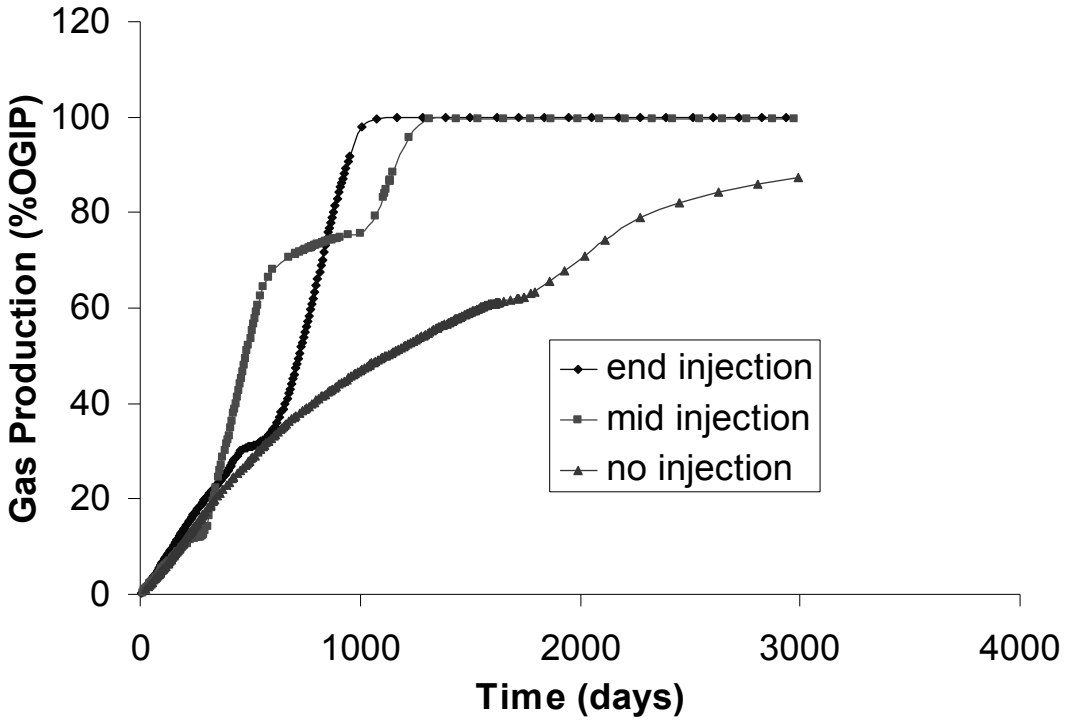

Figure 2: Gas production for the dipping reservoir for 2MPa production pressure, 20MPa injection pressure, and 30°C injection temperature

Figure 4 shows the saturation and temperature profiles at 428 days for the mid injection case. Initially the production is due to depressurization near the production well. The warm water that is injected into the hydrate zone (point M in Figure 1) dissociates the hydrates nearby and the gas and water move up towards the production well. When the dissociation front originating at the production well due to depressurization and the dissociation front originating at injection well due to thermal stimulation meet, the production rate increases. Figure 4 shows the profiles when the fronts have met each other. The production rate increases because gas can flow easily and more energy is injected in to the reservoir through increased injection of warm water. The dissociation rate again decreases at about 600 days. This happens when all the hydrates above the injection well have dissociated, but there is hydrate below the injection well. Warm water takes about 1000 days to warm up the bottom region and then gas production rate increases again, as shown in Figure 2.

In the end injection case the warm water is injected in the water layer at point E in Figure 1. In the first 500 days, hydrates dissociate near the production well due to depressurization without being affected by the injection warm water. The water flows up the structure is very small due to the low water permeability in the hydrate region. When the depressurization front meets the warm water front, the warm water flow up structure increases, which increases the rate of gas production (at about 580 days, as shown in Figure 2). Figure 5 shows the saturation and temperature profiles at 581 days. Hydrates have dissociated from the top part of the reservoir at this time. The injected warm water moves up towards the production well because of the dissociation of the hydrate on the top side of the reservoir. The warm water heats up the middle part of the reservoir which helps in hydrate dissociation. As the injection point of the warm water moves down the reservoir, the start of the high gas recovery phase gets delayed, but the time for completion of gas recovery becomes shorter.

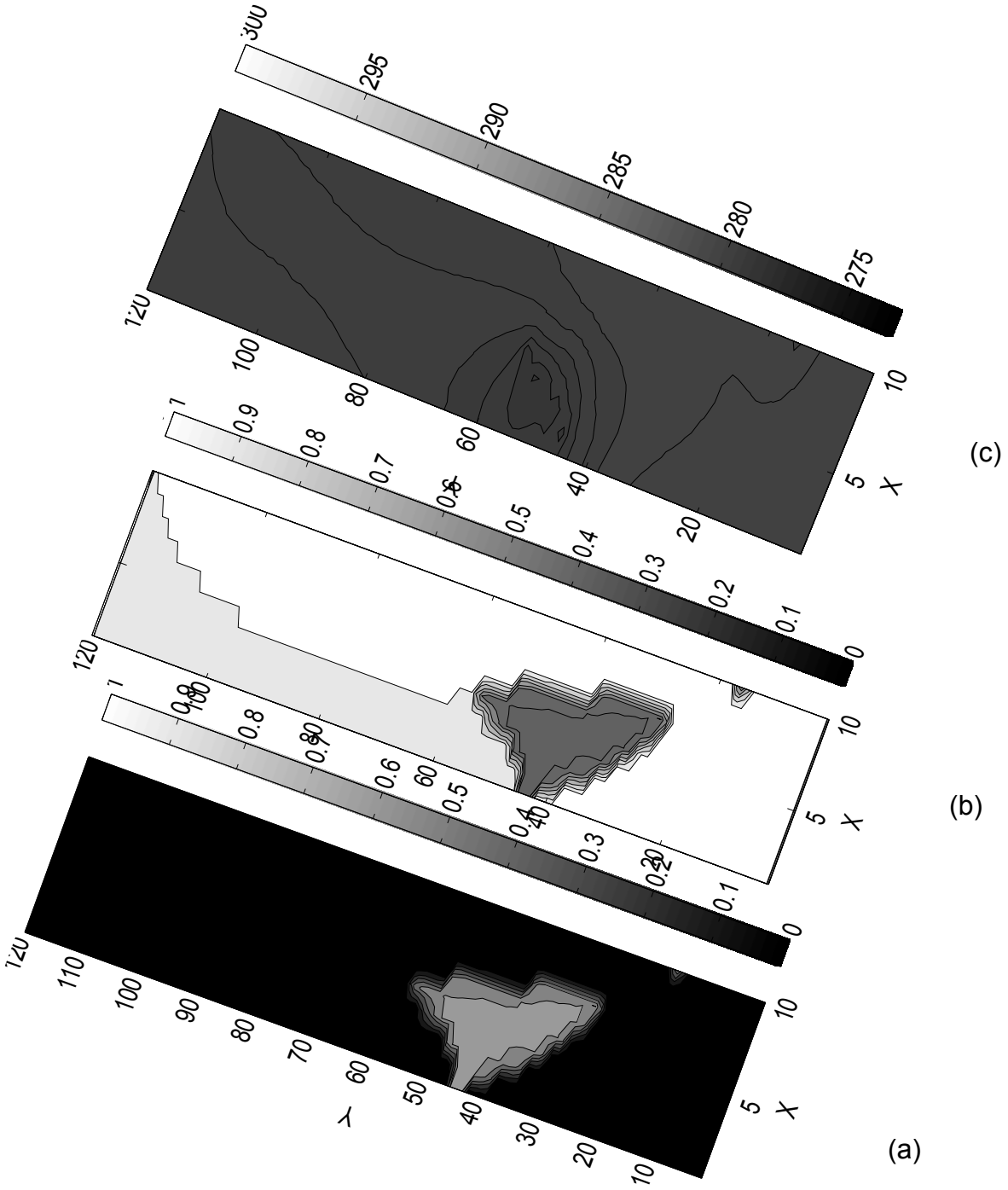

Figure 3: (a) Hydrate saturation profile (b) aqueous saturation profile (c) temperature profile for no injection case after 3000 days

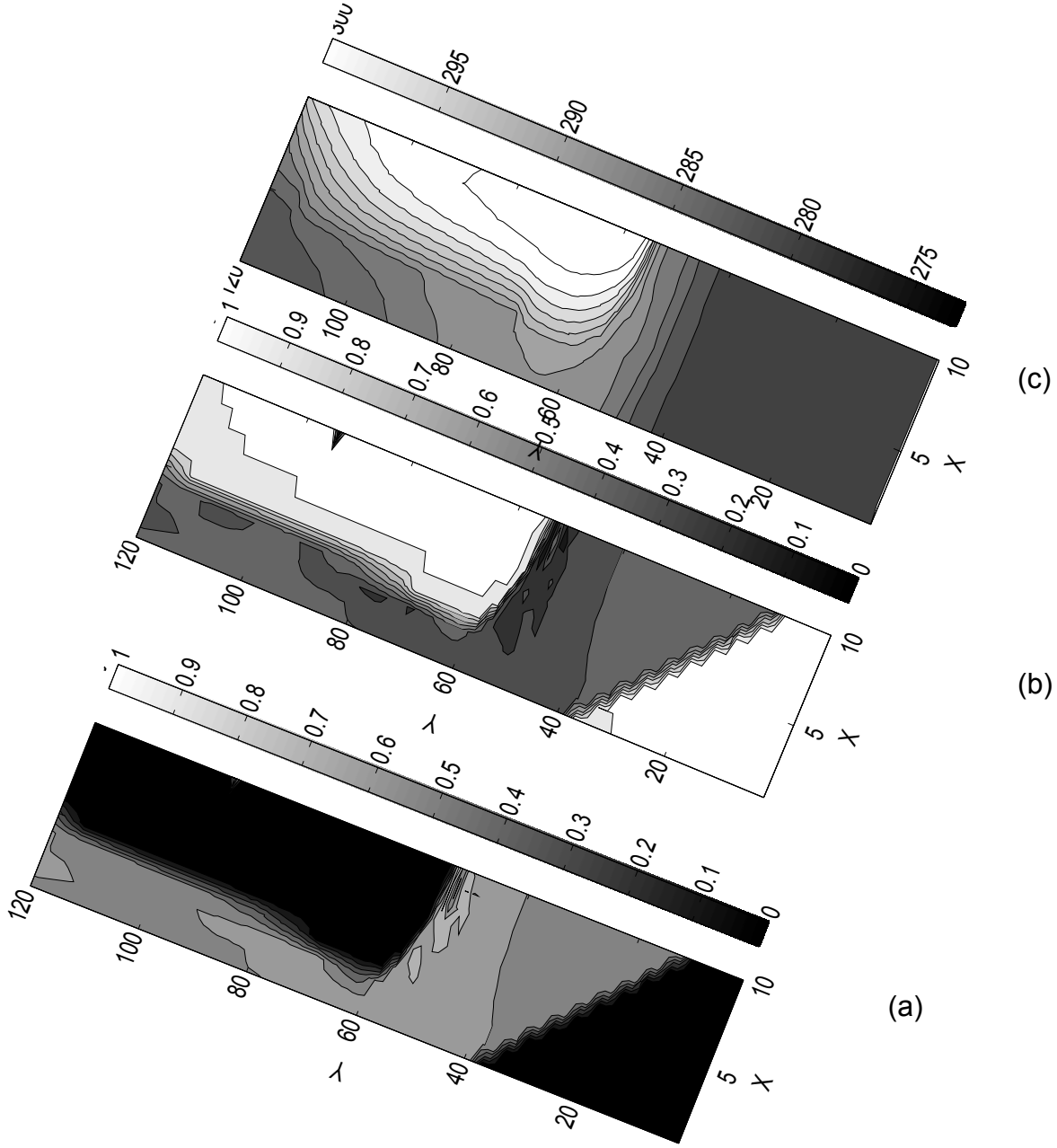

Figure 4: (a) Hydrate saturation profile (b) aqueous saturation profile (c) temperature profile for mid injection case after 428 days

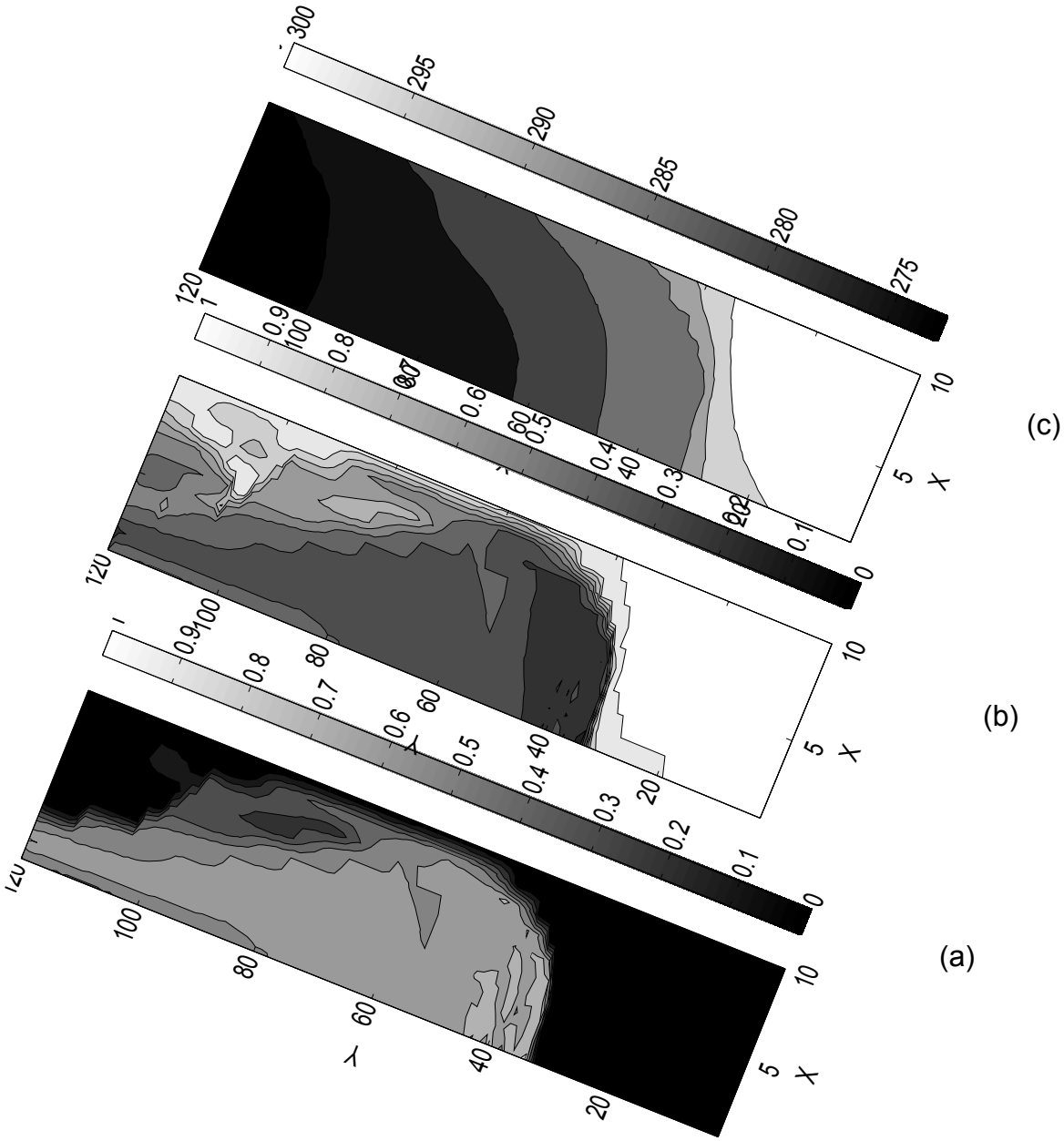

Figure 5: (a) Hydrate saturation profile (b) aqueous saturation profile (c) temperature profile for end injection case after 581 days

Conclusion

Depressurization alone is effective in dipping unconfined reservoirs, but gas production rate is much slower than that for warm water injection. As the injection point of the warm water moves down the reservoir, the start of the high gas recovery phase gets delayed, but the time for completion of gas recovery

becomes shorter. The cost of wells and warm water must be optimized along with the gas production to determine the optimal strategy for producing hydrate reservoirs.

Future Work

Pore scale modeling will be used to find relative permeability of the wetting phase (water) and the non-wetting phase (gas) for different hydrate saturation. The results will be incorporated in the present simulator and production simulation will be done for production strategies of gas hydrates.

Presentations & Publications

1. Phirani, J. (speaker), G. Hirasaki & K. K. Mohanty, “Gas Production from Unconfined Hydrate Reservoirs,” AGU Fall Meeting, San Francisco, December 10-14, 2008.
2. Phirani, J., Pitchumani, R. & Mohanty, K. K., "History Matching of Hydrate Formation-Dissociation Experiments in Porous Media," SPE 118900, Proceedings of the SPE Reservoir Simulation Symposium, Woodlands, TX, February 2-4, 2009.
3. Phirani, J. & Mohanty, K. K., “Warm Water Flooding of Confined Gas Hydrate Reservoirs,” *Chem. Eng. Sci.*, 64, 2361-2369 (2009). doi:10.1016/j.ces.2009.02.019

Task 8: Seafloor and Borehole Stability: Hugh Diagle and Brandon Dugan

Summary
We are moving forward on Task 8 as scheduled. Major advancements have been made on two fronts: (1) modeling (in)stability by looking at active fracture genesis in hydrate settings; and (2) modeling (in)stability by including slope stability calculations during hydrate accumulation (Task 6). In addition to this, we have continued to characterize the permeability behavior of fine-grained sediments including anisotropy and assessing the value of NMR-based permeability estimates in hydrate systems. Other hydrate related activities have been participation in DOE-sponsored site survey analysis for JIP drilling, review of hydrate manuscripts, and presentations at international meetings.

Subtask 8.1: Sediment-Hydrate Properties
Overview
We continue to measure permeability and permeability anisotropy in fine-grained sediments that are representative of those from hydrate settings like the Gulf of Mexico. We hope to establish trends that will be valuable for inputs to hydrate models (Task 6, Task 7) as simulations have shown that anisotropy can affect the distribution of hydrate and production strategies.

Approach
Dead-weight consolidation experiments are used to take sediment mixtures to a known overburden stress. Sub-samples are then selected for vertical permeability measurements, horizontal permeability measurements, and NMR analysis. This provides new data on how permeability anisotropy evolves with increasing overburden stress (or burial) and additional data on our work to evaluate the ability of NMR data to constrain permeability in fine-grained sediments. Permeability is measured both through consolidation experiments and flow through permeability tests. This provides additional information on compression behavior of these sediments.

Results and Discussion
The NMR work has resulted in multiple presentations and one publication. We have limited data on anisotropy with preliminary results suggesting that mechanical compaction yields small amounts of anisotropy by 100m burial depth. Additional tests are necessary to assess how robust these results are and how they may be influenced by mineralogy.

Subtask 8.2: Modeling (In)stability
Overview
We are assessing sediment stability in hydrate systems through two different approaches. In the first, we are using infinite slope stability analysis in our geologic accumulation models (Task 6). This is the first step in trying to address the evolution of geohazards related to hydrate systems. This technique is computationally inexpensive, applicable in geologic and reservoir models, and

provides a quick look at stability to identify locations for detailed stability analysis. The second stability analysis evaluates fracture genesis in fine-grained sediments to assess the condition for failure (fracture) and how that relates to fracture-hosted hydrate. This work is motivated by in situ observations of hydrate filled fractures in fine-grained settings (e.g., Gulf of Mexico, Cascadia, India). This builds upon previous models that look at how hydrate fills fractures (Nimblett and Ruppel, 2003) by addressing the feedbacks between fluid flow, hydrate accumulation, and fracture genesis.

Slope Stability Models

Our basin-scale models of fluid flow have been coupled to a slope stability calculation. These models have been validated and are being included in the hydrate models (beginning with Task 6). For a quick assessment of slope stability evolution, we calculate the factor of safety (FS) using an infinite slope approximation (Equation 8.1) (e.g., Lambe and Whitman, 1969; Dugan and Flemings, 2002).

$$FS = \frac{c' + \left[(\sigma_v - \rho_w g z)\cos^2\theta - P^*\right]\tan\phi_f'}{(\sigma_v - \rho_w g z)\sin\theta\cos\theta} \quad . \qquad \text{(Equation 8.1)}$$

Factor of safety (FS) >1 represents a stable slope and FS≤1 represents an unstable slope. Sediment cohesion for effective stress (c'), total vertical stress (σ_v), hydrostatic pore pressure ($\rho_w gz$), seafloor slope angle (θ), angle of internal friction for effective stress (ϕ_f'), and overpressure (P^*) are required to assess stability. Total vertical stress, hydrostatic pore pressure, and overpressure are calculated in the hydrate accumulation model (Task 6). We assume cohesion is 0 and angle of internal friction is 26° for effective stress conditions based on average values for marine sediments. We use a constant seafloor slope angle of 2° based on the regional seafloor gradient. These parameters can be updated for specific hydrate settings now that the model has been tested.

We completed two quality control tests on the FS calculation where pressure fields are simple (nearly hydrostatic) even in the presence of lithologic heterogeneity. In the first case, we evaluated stability for a 2D hydrate system that included a dipping sand layer where hydrate preferentially accumulates (Figure 8.1). The second case calculated FS in a 2D hydrate system with a vertical fracture (Figure 8.2). These models show two key results: (1) high factors of safety throughout the model domain; and (2) that permeability heterogeneity influences stability. The high FS values are controlled by the low overpressures in this base case and were used to validate the numerical computations as they are consistent with other stability analyses of hydrostatic systems. The influence of permeable conduits is also consistent with previous studies (e.g., Dugan and Flemings, 2002); coupled with the influence of permeable conduits on hydrate saturation, this could be crucial to understand slope stability in hydrate settings. We will explore the feedbacks between permeability, hydrate accumulation, and slope stability.

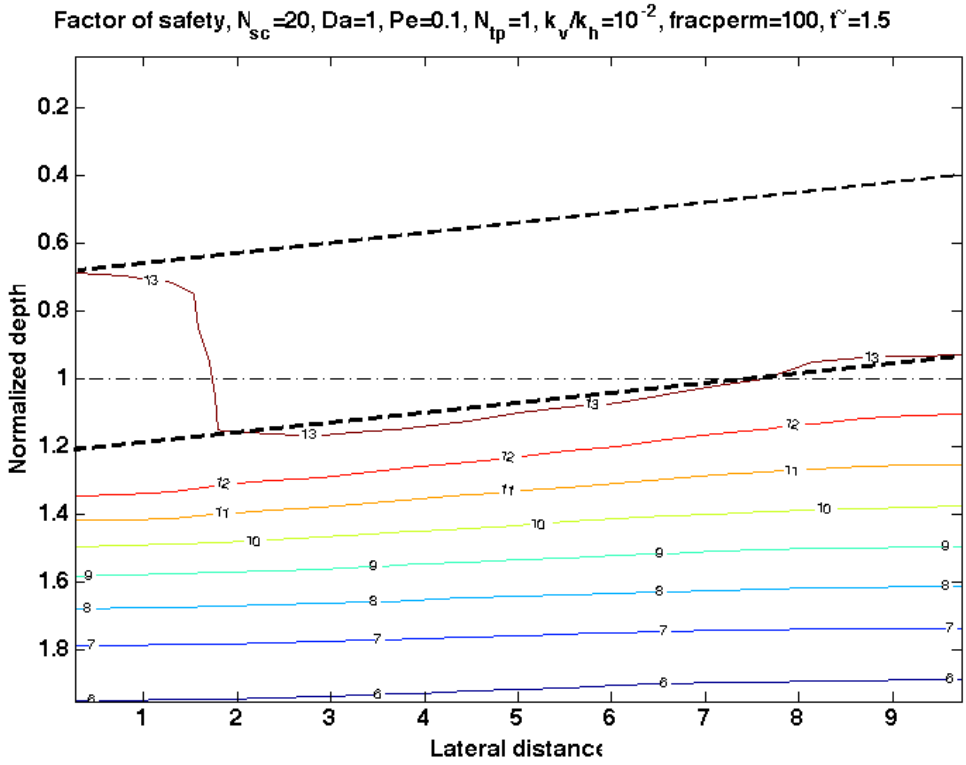

Figure 8.1. Factor of safety contour plot for a 2D hydrate system that has a dipping, permeable sand layer bounded by low permeability clay (Task 6). High FS indicate stable conditions controlled by low overpressure. Future evaluations will look at how changes in pressure and hydrate saturation in sand affect stability. Dashed lines delineate the top and bottom of the sand layer.

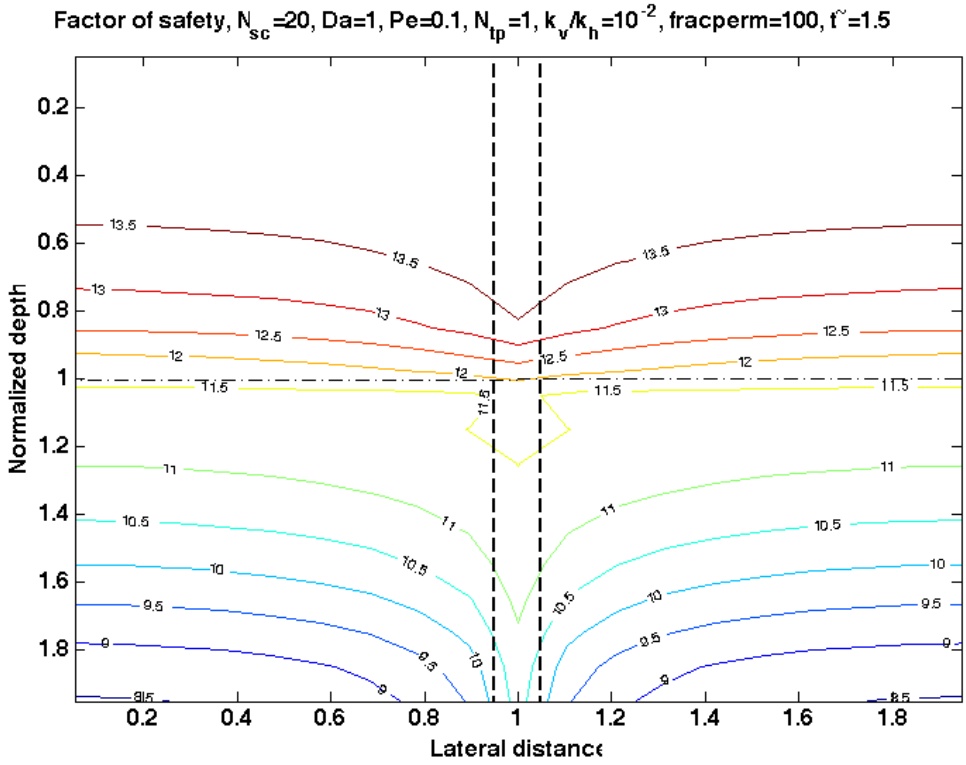

Figure 8.2. Factor of safety contour plot for a 2D hydrate system that has a vertical fracture bounded by low permeability clay (Task 6). High FS indicate stable conditions controlled by low overpressure. Future evaluations will look at how changes in pressure and hydrate saturation in fracture affect stability. We also will look at dynamic genesis of fractures and how this influences hydrate saturation and stability. Dashed lines delineate the boundary of the fracture which is centered on lateral distance = 1.

Another aspect of this modeling will be to evaluate how the stability parameters (friction angle, cohesion) vary with lithology and hydrate saturation. Some of these data exist (Subtask 8.1) however they are limited. We will continue to search the literature for other stability data and will run sensitivity studies and parameter to isolate the key driving forces for unstable conditions. There will be dynamic interactions between hydrate saturation, which will increase cohesion and friction angle and thus increase stability, but can also influence overpressure and decrease stability.

The infinite slope analysis is appropriate for addressing stability of slopes where failure can be considered in one dimension, such that the failure is thin, parallel to the seafloor and edge effects can be neglected wide. This approximation provides a reliable stability calculation for regional slope failures. This simple assessment can identify potentially unstable regions that may require more advanced failure analysis, such as for deep-seated rotational failures (e.g., Bishop 1955). Thus our analysis provides an initial stability calculation and identifies regions that warrant detailed stability calculations.

Fracture Genesis and Porous/Fracture Flow

We have been modeling hydrate formation in pores and fractures in order to determine the conditions under which dual pore- and fracture-hosted hydrate deposits form. Our preliminary work has focused on steady-state systems with fixed rates of fluid flux. Methane concentration in the fluid is assumed to be high enough for hydrate to form when the fluid enters the hydrate stability zone. The rate of hydrate formation is

$$\frac{\partial S_h}{\partial t} = \frac{1}{\phi\left(\rho_h M_h - \rho_f M_{sl}\right)}\left(\phi\rho_f D_m \frac{d^2 M_{sl}}{dz^2} - q_f \frac{dM_{sl}}{dz}\right) \quad , \qquad \text{(Equation 8.2)}$$

where S_h is methane hydrate saturation (fraction of pore volume occupied by hydrate), ϕ is porosity, ρ_h is hydrate bulk density, M_h is mass fraction of methane in the solid phase, ρ_f is fluid density, M_{sl} is methane solubility, D_m is the diffusion-dispersion coefficient, and q_f is fluid mass flux rate (Xu and Ruppel, 1999). We assume that hydrate coats the pore walls as it forms, thus reducing permeability and causing an increase in fluid pressure in order to maintain the constant fluid flux rate. The model is run until the fluid pressure builds up to a point at which hydraulic fractures will form; this point is assumed to be when fluid pressure exceeds 90% of the overburden stress (Finkbeiner et al., 2001). Fractures are assumed to form an equally-spaced fracture system with a finite initial aperture. We assume that hydrate is deposited on the walls of the fractures and that pressure will build up again as the fractures are occluded.

We have run several different scenarios designed to model Hydrate Ridge, Blake Ridge, and Keathley Canyon Block 151, which are three well-characterized study areas where hydrate has been observed in pores and fractures. For Blake Ridge and Keathley Canyon Block 151 we assumed fluid flux rates of 0.3 mm/yr as constrained by field observations (Egeberg and Dickens, 1999; Dugan, 2008). Fluid flux at Hydrate Ridge is much more rapid, between 30 and 100 cm/yr (Torres et al., 2002). Using these parameters, we found that fractures formed after 7.4 million years at Blake Ridge and 7.9 million years at Keathley Canyon Block 151; fractures formed after 344 years at Hydrate Ridge with a fluid flux rate of 100 cm/yr (Figure 8.3). The hydrate saturation at the point of fracture was found to be a function of permeability and fluid flux rate; the higher permeability at Blake Ridge (k = 7x10^{-16} m^2) required S_h in excess of 95% to fracture, while at Keathley Canyon Block 151 (k = 5x10^{-18} m^2) S_h only needed to be ~53%, and the high fluid flux rate at Hydrate Ridge (k = 5x10^{-15} m^2) produced fractures with S_h < 7% (Figure 8.4).

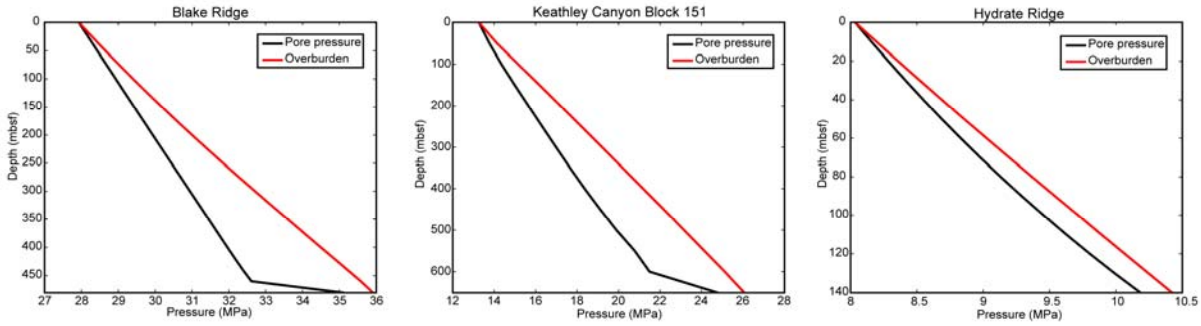

Figure 8.3. Pore pressure at the point of fracturing for the three different environments we modeled. Fracturing was assumed to occur when the fluid pressure reached 90% of the overburden. Overburden was calculated by integrating bulk density. Time to fracture was 7.4 million years at Blake Ridge (left), 7.9 million years at Keathley Canyon Block 151 (middle), and 344 years at Hydrate Ridge (right).

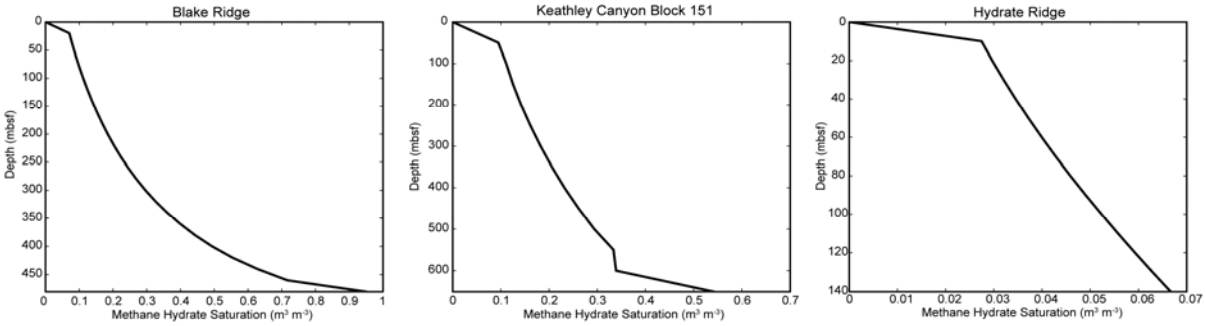

Figure 8.4. Methane hydrate saturation profiles at the point of fracturing for the three different environments we modeled. The hydrate saturation necessary to produce fractures varies with permeability and fluid flux.

Our results illustrate conceptually how fractures may arise due to increased pressures associated with hydrate formation, but the time scales necessary to produce these pressures are much longer than seems reasonable. We therefore plan to investigate other modes of fracturing such as dilation or Mohr-Coulomb fractures, as well as transient higher fluid flux rates and variable pressure conditions. We also must explore other controls on hydrate formation such as the presence of free gas, permeability variation due to fractures, and variable and transient fracture opening/spacing. Eventually these fracture models will be coupled with the geologic hydrate accumulation models (Task 6).

Subtask 8.3: Integrating geomechanical studies

Overview

This subtask involves assessing ongoing geomechanical studies to maximize our understanding of geomechanical properties of hydrate bearing sediments across DOE-funded projects. The goal is a comprehensive geomechanical database and modeling approach with a means to understand these properties at geologic and human time-scales. One major accomplishment for this project have been development of a review paper on physical properties of hydrate bearing sediments (Waite et al., in review) that integrates numerous DOE and other studies defining the state of knowledge on sediment-hydrate properties and the key data gaps (primarily data on low hydrate saturation in sediments). Another

advancement on this front has been the development of our fracture genesis model (Subtask 8.2). This model will provide complementary data for other DOE studies looking at geomechanical properties (DE-FC26-05NT42664/ESD05-036 - Geomechanical Performance of Hydrate-Bearing Sediments in Offshore Environments) and fractures in hydrate systems and how they relate to the presence of free gas within the hydrate stability region (DE-FC26-06NT43067 - Mechanisms Leading to Co-existence of Gas and Hydrate in Ocean Sediments).

Hydrate Presentations

Chatterjee, S., Bhatnagar, G., Chapman, W.G., Dickens, G.R., Dugan, B., Hirasaki, G.J., 2008, Effect of Lithologic Heterogeneities on Gas Hydrate Distribution, *AGU 2008 fall meeting*, San Francisco, CA.

Daigle, H.C., Dugan, B., 2008, Extending Nuclear Magnetic Resonance Data for Permeability Estimation in Fine-Grained Sediments, *AGU 2008 fall meeting*, San Francisco, CA.

Hustoft, S., Dugan, B., Mienert, J., 2008, Integrated Hydrological Flow-Modeling and 3D Seismic Analysis of the Nyegga Pockmark-Field at the Mid-Norwegian Constrain Times of Methane Leakage, *Subsurface Sediment Remobilization and Fluid Flow in Sedimentary Basins Conference* (The Geological Society), 21-22 October 2008, London, England.

Hydrate Activities

DOE/IODP Hydrate Drilling [Aug 2008 – present] – Dugan has been working on evaluation of hydrate-related drilling hazards in the Gulf of Mexico and how existing and new drilling techniques could be used to facilitate DOE/JIP drilling of hydrate in the Gulf with the IODP drillship

DOE/JIP Site Selection Working Group member [2007-present]

Geofluids Editorial Board member [2007-present]

Reviewer of hydrate-related manuscripts for Marine and Petroleum Geology, Journal of Geophysical Research, and Basin Research

Steering Committee member for IODP Charting the Future Course of Scientific Ocean Drilling (CHART) Workshop

Publications

Daigle, H., Dugan, B., 2009, Extending NMR data for permeability estimation in fine-grained sediments, *Marine and Petroleum Geology*, doi:10.1016/j.marpetgeo.2009.02.008.

Hustoft, S., Dugan, B., Mienert, J., accepted, Effects of rapid sedimentation on developing the Nyegga pockmark-field; constraints from hydrological modeling and 3D seismic data, offshore mid-Norway, *Geochemistry, Geophysics, and Geosystems*.

Waite, W., Santamarina, C., Cortes, D., Dugan, B., Espinoza, N., Germaine, J., Jang, J., Jung, J., Kneafsey, T., Shin, H., Soga, K., Winters, W., Yun, T-S., in review, Physical Properties of Hydrate-Bearing Sediments, *Reviews of Geophysics*.

References

Bishop, A.W., 1955, The use of the slip circle in the stability analysis of earth slopes, *Geotechnique*, 5, 7-17.

Dugan, B., 2008, Fluid flow in the Keathley Canyon 151 Mini-Basin, northern Gulf of Mexico, *Marine and Petroleum Geology*, 25, 919-923, doi:10.1016/j.marpetgeo.2007.12.005.

Dugan, B., Flemings, P.B., 2002, Fluid flow and stability of the US continental slope offshore New Jersey from the Pleistocene to the present, *Geofluids*, 2,137-146.

Egeberg, P.K., Dickens, G.R., 1999, Thermodynamic and pore water halogen constraints on gas hydrate distribution at ODP Site 997 (Blake Ridge), *Chemical Geology*, 153, 53-79.

Finkbeiner, T., Zoback., M., Flemings, P., Stump, B., 2001, Stress, pore pressure, and dynamically constrained hydrocarbon columns in the South Eugene Island 330 field, northern Gulf of Mexico, *AAPG Bulletin*, 85(6), 1007-1031.

Lambe, T.W., Whitman, R.V., 1969, Soil Mechanics, John Wiley & Sons, New York, 553pp.

Nimblett, J., Ruppel, C., 2003, Permeability evolution during the formation of gas hydrates in marine sediments, *Journal of Geophysical Research*, doi:10.1029/2001JB001650.

Torres, M.E., McManus, J., Hammond, D.E., de Angelis, M.A., Heeschen, K.U., Colbert, S.L., Tryon, M.D., Brown, K.M., Suess, E., 2002, Fluid and chemical fluxes in and out of sediments hosting methane hydrate deposits on Hydrate Ridge, OR, I: Hydrological provinces, *Earth and Planetary Science Letters*, 201, 525-540.

Xu, W., Ruppel, C., 1999, Predicting the occurrence, distribution, and evolution of methane gas hydrate in porous marine sediments, *Journal of Geophysical Research*, 104(B3), 5081-5095.

Task 9: Geophysical Imaging of Gas Hydrate and Free Gas Accumulations
P. Jaiswal and C.A. Zelt

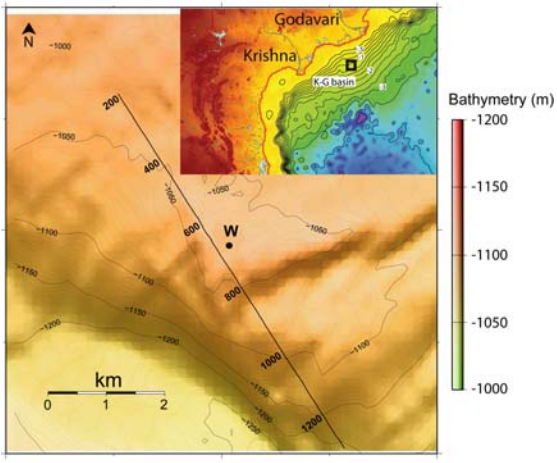

Figure 1. Basemap. Seismic line is indicated in black line with CDPs labeled in multiples of 200. Location of the Well W is indicated in solid dot. Bathymetry is labeled every 50m. Location of the study area with respect to India is shown in inset with rivers Krishna and Godavari labeled. Bathymetry is labeled in km.

The traveltime inversion part of the project is complete. The final results were shown at the US-Korea Methane Hydrate Workshop at Lawrence-Berkeley lab on April 28, 2009. We present the same series of results below. The final traveltime model will be used as a starting model for waveform inversion which is our goal in year 2.

Arrival times from five geological interfaces, including the seafloor and the bottom simulating reflector (BSR) were inverted to obtain the final traveltime model (Figure 2). Figure 2 was obtained by inverting 101 shots evenly spaced along the model 62.5 m apart (every 5th shot). All shots have a near and a maximum offset of 70 and 1500 m respectively. The initial model for traveltime inversion was constructed using stacking velocity analysis (Stack: Figure 3). Pre-stack depth migration (PSDM) of the multi-channel seismic (MCS) data using the final traveltime model yielded the final depth image (Figure 4). The bottom simulating reflector appears fairly distinctly in both the stack and the PSDM (Figure 3 and 4). The seafloor reflections were inverted independently to obtain the variation of the velocity in the water column (Figure 5).

A feature relevant to understanding the gas-hydrate distribution along the seismic line appears to be a mound between CMPs 450-700 (Figures 3 and 4). The BSR appears to have diminished reflectivity below the mound. The mound appears to be bounded by normal faults on both sides. Detailed interpretation is in progress. Seawater velocity appears to be laterally decreasing above the mound. The significance of the water velocity structure (Figure 5) is currently being discussed with our colleagues at the National Institute of Oceanography, India. The vertical and lateral variations could be reflective of local currents,

salinity, and temperature gradients. It could also be reflective of the gas-seepage from the mound.

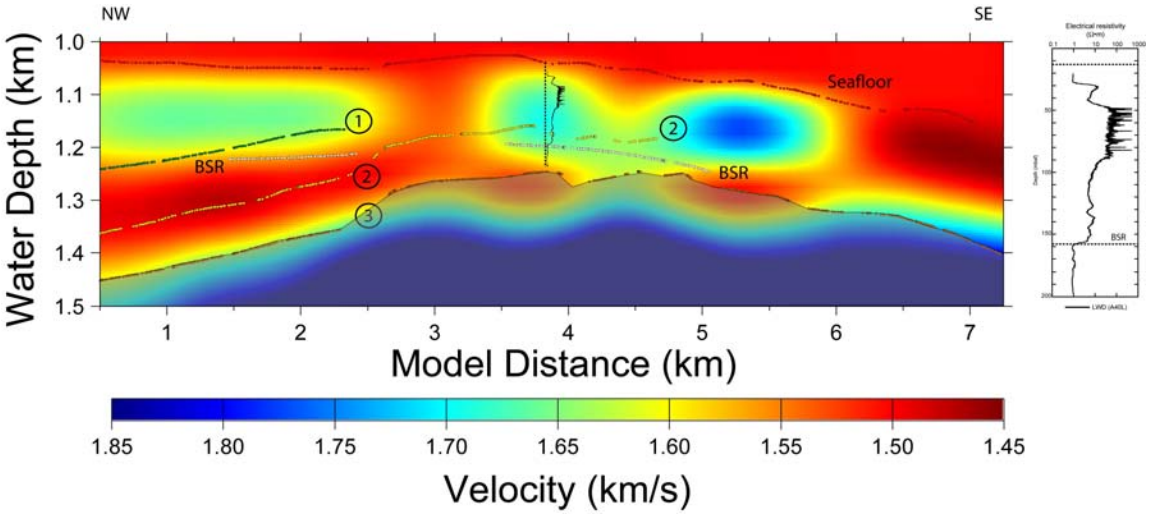

Figure 2. Velocity Model. Seafloor and BSR along with three horizons (1, 2, and 3) that are used for traveltime inversion are labeled. The sediment velocity above horizon three seems to be ~1.5 km/s. Regions of enhanced velocity above BSR suggest presence of hydrates. P-wave log is overlaid at the appropriate location. Parts of the model not covered by reflections are masked.

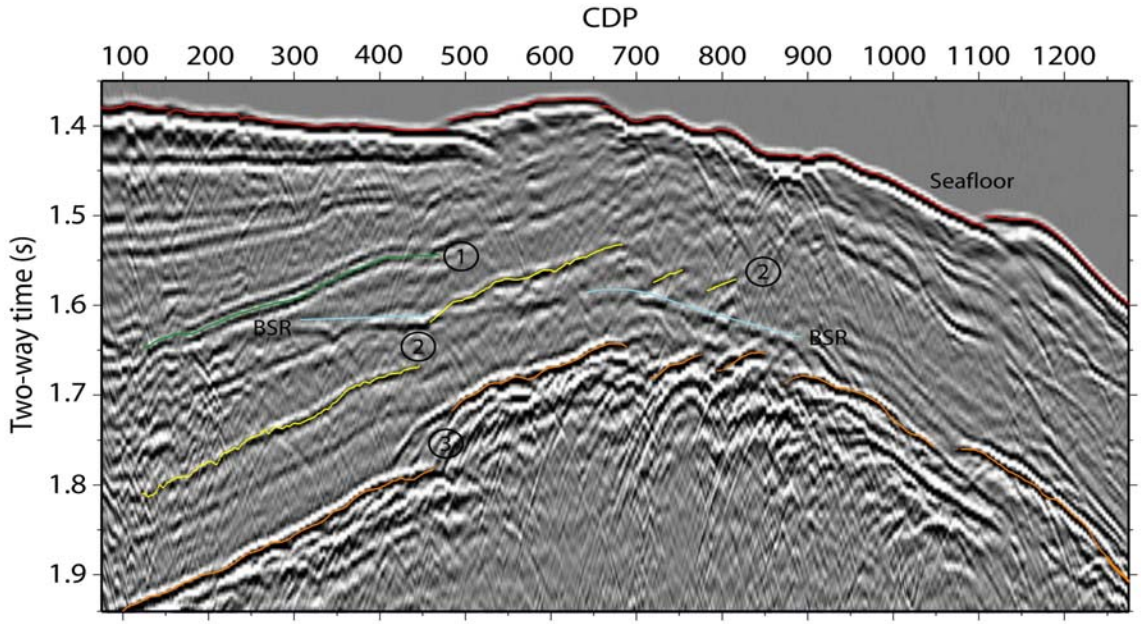

Figure 3. Stack data. Seafloor and BSR along with three horizons (1, 2, and 3) that are used for traveltime inversion are labeled.

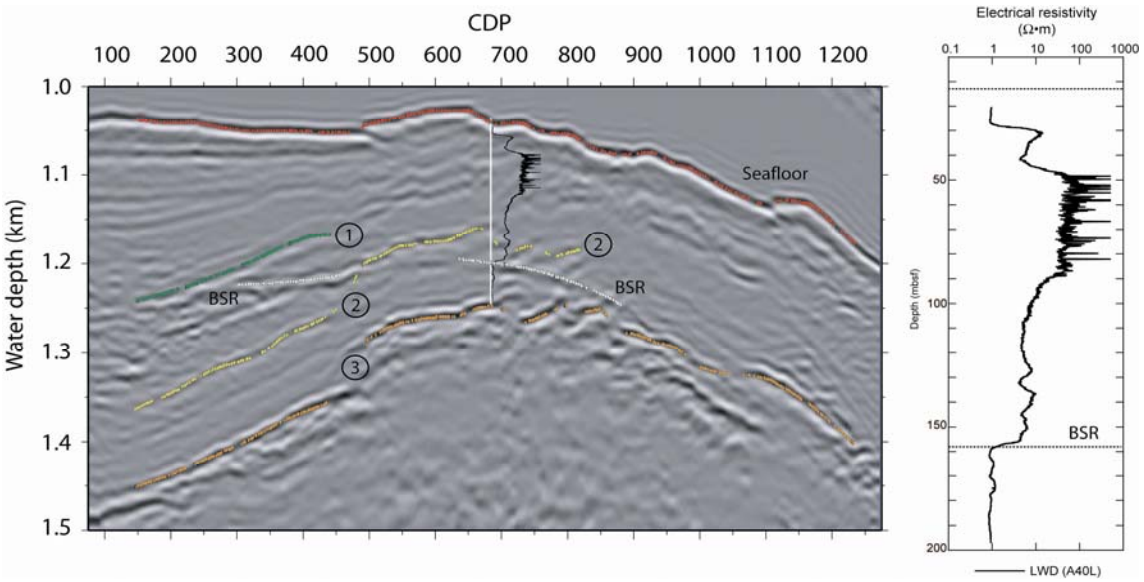

Figure 4. Pre-Stack depth migrated image. Seafloor and BSR along with three horizons (1, 2, and 3) that are used for traveltime inversion are labeled. Trajectory of W (Figure 1) is indicated with a solid white line. Also displayed is the resitivity log along the trajectory. Note the BSR in the log well coincides with the BSR in the migrated image suggesting that the velocity model from traveltime inversion is reliable.

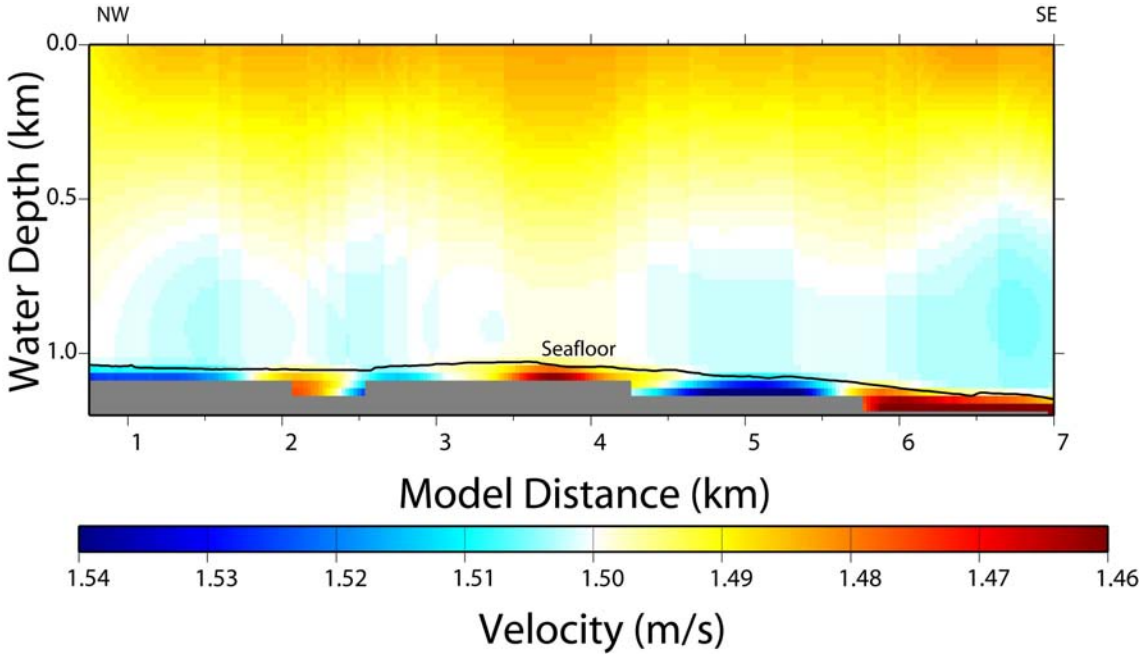

Figure 5. Velocity variation in the water startigraphy. The mound occurs between model distance 3 and 4.25 km. Assuming a normal water velocity of 1.5 km/s, velocities lower and higher than 1.5 km/s are displayed in shades of red and blue respectively. Seafloor is indicated with a solid black line.

The data appears to be resolving perturbations of the order of 1% in Figure 5. Checkerboard resolution test (Figure 6) with 1% anomaly strength was performed to ensure that the velocity variations in Figure 5 are genuine.

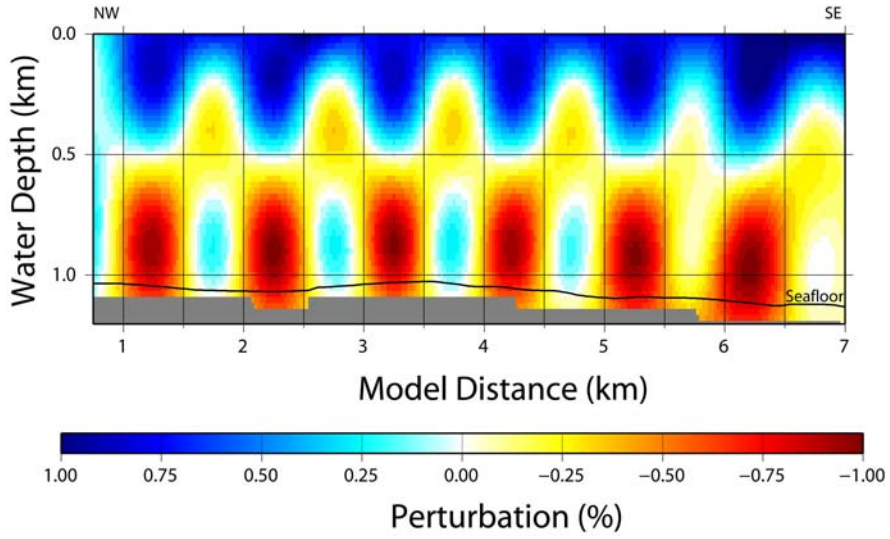

Figure 6. Checkerboard resolution test. The pattern has 0.5 X 0.5 km dimension and 1% strength. The data coverage appears to be successfully resolving the checkerboard pattern. Seafloor is indicated with a solid black line.

Seafloor reflection arrivals were inverted using uncertainties of 4 ms (twice the recording sample interval). The reliability of the seawater model was also assessed by comparing the observed and the predicted traveltimes from the seawater model (Figure 5). The comparison shows that the predicted treltimes have a uniform distribution with offset (Figure 7a), and are unbiased (Figure 7b).

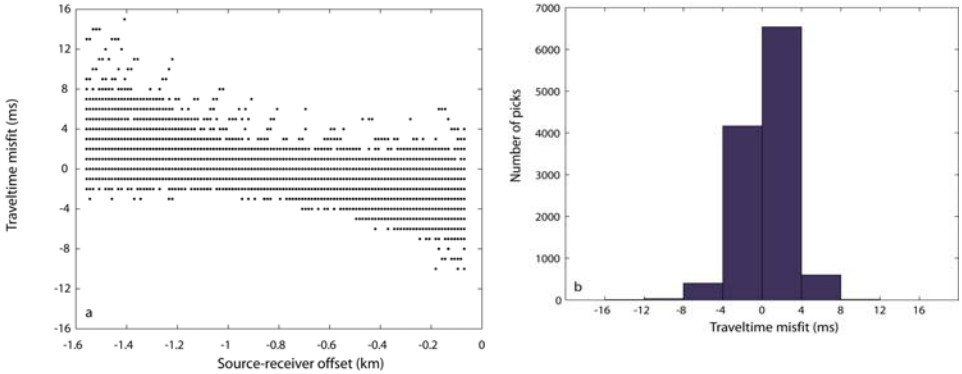

Figure 6. Traveltime misfit. a) Traveltime misfit distribution with offset. b) histogram of travletime misfit. a) and b) together suggest that most of the traveltime picks have been fit to within their assigned uncertainty of 4 ms. Misfit of a relatively fewer (< 1000) number of picks are greater than 4 ms.

Task 10 Technology Transfer

US – Korea Methane Hydrate Workshop; April 28-29, 2009

Delegates: Jerry Dickens, Pryank Jaiswal, George Hirasaki

Abstracts of presentations/posters the AGU meeting in San Francisco, December, 2008

Gas Production from Unconfined Hydrate reservoirs

J. Phirani, G. J. Hirasaki, K. K. Mohanty

Description of material: Large quantities of natural gas hydrates are present in marine sediments along the coastlines of many countries as well as in the arctic region. The production of gas from these naturally occurring gas hydrates is difficult due to complexity of thermodynamics and fluid flow involved in the process. This research is aimed at assessing production of natural gas from unconfined marine deposits of methane gas hydrates. An implicit, multiphase, multi-component, thermal, 3D simulator is used which can simulate formation and dissociation of hydrates in porous media in both equilibrium and kinetic modes. Three components (hydrate, methane and water) and four phases (hydrate, gas, aqueous-phase and ice) are considered. In this work we simulate depressurization and warm water flooding for gas production from hydrates in reservoirs underlain by an unconfined aquifer layer. Water flooding has been studied as a function of injection temperature, injection pressure, production pressure and degree of unconfinement.

Application: In order to produce gas from hydrates economically, efficient production techniques must be developed. Experiments on hydrates are difficult to perform; feasibility of production can be found from simulations. Hydrate reservoirs associated with unconfined aquifer beneath are not uncommon. The determination of injection and production conditions for these reservoirs through simulation will help in designing the effective production techniques.

Results and discussion: For the unconfined reservoirs associated with large aquifers the production by depressurization is inefficient. Water from the aquifer maintains the pressure in the reservoir except in the near-well regions. Warm water flooding is very effective in hydrate dissociation. Sensitivity of gas production to injection and production well conditions and degree of un-confinement has been studied.

Significant new contribution: Production strategies for unconfined hydrate reservoirs.

Effect of Lithologic Heterogeneities on Gas Hydrate Distribution

Sayantan Chatterjee, Gaurav Bhatnagar, Walter G. Chapman, Gerald R. Dickens, Brandon Dugan, George J. Hirasaki

Accumulation of gas hydrate and free gas is modeled in heterogeneous marine sediments over geologic time scales. Our two-dimensional models incorporate deposition and compaction of heterogeneous sediment, methane

generation, and migration of water with dissolved gas, so we can study how focused fluid flow through a vertical fracture network and/or high permeability sand layers affects regional and local hydrate accumulation and saturation. The focused fluid flow is visualized by vector field plots. Simulations with a vertical fracture network, 100 times more permeable than the surrounding formation that extends through the gas hydrate stability zone (GHSZ) up to the seafloor show focused fluid flow causing relatively higher hydrate and free gas saturation within the fracture network compared to the surrounding, lower permeability formation. Systems with dipping sand layers show similar localized, enhanced concentrations of hydrate and free gas within the high permeability conduits. Anisotropic cases with lower ratio of vertical to horizontal permeability, k_v/k_h (order of 10^{-2}), show relatively higher hydrate saturations within the high permeability conduits because anisotropy focuses more of the fluid into the high permeability conduit. Cases where vertical fracture networks cut through sand beds will also be discussed. In our previous **one-dimensional** work, we found that the accumulated hydrate saturation was dependent on Peclet number, Pe, which is the ratio of convective flux to the diffusive flux of methane. In our current two-dimensional work, it is the **local** convective flux relative to diffusion that determines the magnitude of hydrate and free gas saturation.

Extending Nuclear Magnetic Resonance Data for Permeability Estimation in Fine-Grained Sediments

Hugh Daigle and Brandon Dugan, Department of Earth Science, Rice University, Houston, Texas, USA

We developed a method for using nuclear magnetic resonance (NMR) T_2 data and gamma ray data to estimate lithology-dependent permeability in silt- and clay-rich sediments. This model, based on the Schlumberger-Doll Research (SDR) model, allows for high resolution (<1 m) permeability estimates throughout a logged interval. Our model was calibrated using direct measurements on core samples from Keathley Canyon Lease Block 151 in the northern Gulf of Mexico. From NMR and gamma ray data we are able to determine permeability from 10^{-18} to 10^{-14} m^2 (0.001 to 10 millidarcies). Thus from discrete core samples and log data we were able to develop a permeability model for the entire sedimentary column (425 m). Lithologic variation was incorporated into the model by varying the *A* coefficient based on the gamma ray response. This provides a more accurate permeability model than assigning a constant value to *A* as is typically done. The relationship between *A* and intrinsic lithologic properties is unclear; simple pore system models suggest that *A* may be related to specific surface, tortuosity, and pore structure; we investigate simple models to quantify how these properties vary with sediment consolidation and what their relationship is to *A*. A comprehensive understanding that links NMR data and *A* to pore-scale properties will provide new constraints on deformation and flow in porous systems, and will contribute to our understanding of sediment properties for fluid flow modeling at local and regional scales.

Compositional Effect on Hydrate/Free Gas Transition and BSR

Guangsheng Gu, Priyank Jaiswal, Walter Chapman, Colin Zelt, and George J Hirasaki

Abstract

Gas hydrate is often characterized in remote detection by seismic profiles and Bottom-Simulating Reflector (BSR), which is due to an abrupt acoustic impedance contrast between the base of gas hydrate stability zone (GHSZ) and free gas layer below. However, in some cases, hydrate is present but BSR is not observed. We hypothesize that multi-hydrocarbon components in a hydrate system can induce gradual transition of hydrate/free gas saturations, and result in a weak seismic reflection.

In this work, we demonstrate that a small fraction of heavier hydrocarbon component can induce a gradual transition of hydrate/free gas saturations in sediment over a significant distance (relative to acoustic wavelength). If the thermogenic gas source from deeper sediment contains 5% (mol/mol) propane, a transition zone as thick as ~50 m can be formed, in which hydrate, gas, and aqueous phases can co-exist. The saturations of each phase change gradually, causing a gradual transition of acoustic impedance. Seismic waves with different characteristic wavelengths are tested to generate synthetic seismic responses. Results show that, if the ratio of characteristic wavelength to thickness of transition zone (λ/L_{trans}) is less than 1, then the reflection is very weak; if the ratio is much higher than 1, the reflection is very strong. This indicates that in the case of a multi-hydrocarbon hydrate system, the reflection response is dependent on the thickness of transition zone and seismic wavelength. This provides a possible mechanism why in some places hydrate is present but BSR is not observed.

COST PLAN / STATUS								
	Phase 1	**Phase 2**	**Phase 3 7/01/008-6/30/09**				**Phase 3**	
Baseline Quarter Reporting			7/1/08 - 9/30/08	10/1/08 - 12/31/08	1/1/09 - 3/31/09	4/1/09 - 6/30/09	Totals	Cumulative Totals
Baseline Cost Plan Allocation (SF- 424A)								
Federal Share	$ 3,624	$ 320,010	$ 82,784	$ 82,784	$ 82,784	$ 82,784	$ 331,135	$ 654,769
Non-Federal Share	$ 1,004	$ 114,612	$ 26,908	$ 26,908	$ 26,908	$ 26,908	$ 107,630	$ 223,246
Total Planned	$ 4,628	$ 434,623	$ 109,691	$ 109,691	$ 109,691	$ 109,691	$ 438,765	$ 878,016
Cumulative Baseline Cost	$ 4,628	$ 439,251	$ 548,942	$ 658,634	$ 768,325	$ 878,016	$ 1,316,781	$ 1,760,660
Actual Incurred Cost								
Federal Share	$ 3,082	$ 298,506	$ 71,995	$ 72,124	$ 61,289			$ 316,637
Non-Federal Share	$ 1,091	$ 118,145	$ 15,049	$ 30,099	$ 29,178			$ 193,562
Total Incurred	$ 4,173	$ 416,651	$ 87,044	$ 102,223	$ 90,467			$ 700,558
Cumulative Costs	$ 4,173	$ 420,824	$ 507,868	$ 610,091	$ 700,558			$ 2,243,514
Variance (plan-actual)								
Federal Share	$ 542	$ 21,504	$ 10,789	$ 10,660	$ 21,495			$ 64,989
Non-Federal Share	$ (87)	$ (3,533)	$ 11,859	$ (3,192)	$ (2,271)			$ 2,776
Total Variance	$ 455	$ 17,971	$ 22,647	$ 7,468	$ 19,224			$ 67,766
Cumulative Variance	$ 455	$ 18,426	$ 41,073	$ 48,541	$ 67,766			

Milestone Plan/Status

Task	Milestone: Status and Results	Date	Status
5. Carbon inputs and outputs to gas hydrate systems	5.1a Measure iodine in sediments We have measured iodine concentrations in pore waters and sediments from 4 gas hydrate systems.	12/07	Done (except writing)
	5.1b Constrain C_{org} inputs from iodine We have measured the content and isotopic composition of organic carbon and carbonate in sediment from cores of several gas hydrate systems. We are beginning to incorporate the results into models.	10/08	Partly Done
	5.2a Construct metal profiles in sediments We have measured metal contents in pore water and sediment from cores of two gas hydrate systems along the Peru Margin and in the Sea of Japan. The Sea of Japan work has been published (Snyder et al., 2007).	12/09	Partly Done
	5.2b Modeling/integrating profiles We are beginning to incorporate the results into models. We have written an article defending our use of the SMT as a proxy for methane loss through AOM.	12/10	Begun

6. Numerical models for quantification of hydrate and free gas accumulations	6.1 Model development. The recipient shall develop finite difference models for the accumulation of gas hydrate and free gas in natural sediment sequences on geologically relevant time scales.	9/07	done

	6.2: Conditions for existence of gas hydrate The recipient shall summarize, quantitatively, the conditions for the absence, presence, and distribution of gas hydrates and free gas in 1-D systems by expressing the conditions in terms of dimensionless groups that combine thermodynamic, biological and lithologic transformation, and transport parameters.	3/07	done
	6.3 Compositional effect on BSR The recipient shall add to the numerical model, developed under this task, a chloride balance and multi-hydrocarbon capability specifically to investigate how hydrocarbon fractionation might affect Bottom Simulating Reflectors (BSRs).	7/07	In Progress
	6.4: Amplitude Attenuation and chaotic zones due to hydrate distribution The recipient shall simulate preferential formation of gas hydrate in coarse-grained, porous sediment in 2-D by linking fluid flux to the permeability distribution.	3/09	started
	6.5: Processes leading to overpressure The recipient shall quantify, by simulation and summarize by combination of responsible dimensionless groups, the conditions leading to overpressure to the point of sediment failure.	3/08	Collaborating with task 8
	6.6 Concentrated hydrate and free gas The recipient shall, using 2-D and 3-D models, simulate lateral migration and concentration of gas hydrate and free gas in structural and stratigraphic traps.	3/08	ongoing
	6.7 Focused free gas, heat and salinity The recipient shall quantify, using 2-D and 3-D model simulations and comparisons to available observations, the factors controlling the process of localized upward migration of free gas along faults and lateral transfer to dipping strata that can lead to chaotic zones and possible accumulations of concentrated hydrate.	9/09	

	6.8 Sulfate profile as indicator of methane flux The recipient shall compute, for systems where data on the sulfate profile is available, the oxidation of methane by sulfate and shall indicate the perceived level of effect on gas hydrate accumulation and the data's value as an indicator of methane flux.	7/07	Revisited to collaborate with Task 5.
	6.9 Application of models to interpretation of case studies. The models developed in Task 6 will be applied to case studies in the interpretation of each of the other tasks.	6/10	started
7. Analysis of production strategy	7.1a Pore scale model development and Hydrate code comparison For this milestone, we will develop pore-scale models of hydrate accumulation by simulation. Our hydrate code will be used to solve a set of problems formulated by the Code Comparison Study group. Our results will be compared with those of other hydrate codes. Should be changed to: 6/08 Reason: The starting date was moved to 6/07 Status: Code comparison study is 80% complete.	1/08	6/08 Code comparison is done.
	7.1b Petrophysical and thermophysical properties of hydrate sediments from pore-scale model For this milestone, we will assume the pore-scale models of hydrate accumulation developed in the last milestone and estimate transport properties as a function of hydrate and gas saturations. Should be changed to: 6/09 Reason: The starting date was moved to 6/07 Status: Have not started	1/09	In progress
	7.2a Modeling of several production strategies to recover gas from marine hydrates Several production strategies would be modelled using the transport property correlations developed in the previous milestone. Optimal strategies will be identified.	1/10	In progress

	Should be changed to: 6/10		
	7.2b Effect of marine reservoir heterogeneities on production of methane Reservoir heterogeneity anticipated in marine environments (known or determined through other tasks) would be incorporated. Appropriate hydrate distributions, either constrained from experimental data or mechanistic simulations (Task 5) would be used. Sensitivity of gas production to the heterogeneities would be calculated. Should be changed to: 6/11 Reason: The starting date was moved to 6/07 Status: Have not started	12/10	6/10
8. Seafloor and borehole stability	8.1a Collection of data We have collected the published data and are working it into a data base. We are also working on a review paper summarizing the state of the art settings. This will include laboratory experiments, field data, published results, and unpublished data.	05/08	Completed
	8.1c Complete database We are organizing the data from task 8.1a into a format that can be searched and used by researchers trying to understand mechanical behavior of hydrate-bearing sediment. We will also identify key gaps in the database for focusing future hydrate research endeavors. We have started exchanging these data with the modeling components of this project.	10/09	On target
	8.2a Link database with models We have started passing data along to the modeling groups so they can use sediment properties from hydrate provinces as they simulate hydrate accumulation and production.	08/08	On target
	8.2b Add sediment stability to models Standard stability calculations have been implemented in a standard basin model. Now that it is functional we will work with the hydrate accumulation model to add a stability	10/08	On target

	calculation to the 2-D models.		
	8.2c Conditions for (in)stability After implementing the stability model in the hydrate accumulation code, we can explore the conditions (e.g., hydrate dissociation, sea-level fall) that could drive slope failure and hydrate/methane release or lead to borehole failures during production.	9/09	On target
9 Geophysical imaging of hydrate and free gas	9.1 Preliminary processing and inversion of seismic data. Perform conventional seismic reflection processing, velocity analysis, travel time tomography, and other analyses as deemed appropriate and necessary.	8/08	Done
	9.2: Final 1-D elastic and 2-D acoustic waveform inversion. Apply 1-D elastic and 2D acoustic inversions on data obtained from subtask 9.1 to derive determine high-resolution elastic and acoustic properties.	8/09	On Target
	9.3: Rock physics modeling. Apply rock physics models to the developed seismic models to estimate hydrate saturation and lithology through application of well log data in conjunction with data from subtask 9.2. For this subtask we shall seek to collaborate with research being conducted under separately funded DOE-NETL projects (DE-FC26-05NT42663 with Stanford University, "Seismic-Scale Rock Physics of Methane Hydrate" and others as applicable).	8/10	On Target

National Energy Technology Laboratory

626 Cochrans Mill Road
P.O. Box 10940
Pittsburgh, PA 15236-0940

3610 Collins Ferry Road
P.O. Box 880
Morgantown, WV 26507-0880

One West Third Street, Suite 1400
Tulsa, OK 74103-3519

1450 Queen Avenue SW
Albany, OR 97321-2198

539 Duckering Bldg./UAF Campus
P.O. Box 750172
Fairbanks, AK 99775-0172

Visit the NETL website at:
www.netl.doe.gov

Customer Service:
1-800-553-7681